minerals

MDPI

Article

Characterization of Fibrous Wollastonite NYAD G in View of Its Use as Negative Standard for *In Vitro* Toxicity Tests

Dario Di Giuseppe [1,*], Valentina Scognamiglio [1], Daniele Malferrari [1], Luca Nodari [2], Luca Pasquali [3,4,5], Magdalena Lassinantti Gualtieri [3,6], Sonia Scarfì [7,8], Serena Mirata [7], Umberto Tessari [9], Miriam Hanuskova [3] and Alessandro F. Gualtieri [1]

1 Department of Chemical and Geological Sciences, University of Modena and Reggio Emilia, Via Campi 103, 41125 Modena, Italy; vscognam@unimore.it (V.S.); daniele.malferrari@unimore.it (D.M.); alessandro.gualtieri@unimore.it (A.F.G.)
2 CNR-ICMATE Institute of Condensed Matter Chemistry and Technologies for Energy, Italian National Research Council, Corso Stati Uniti 4, 35127 Padova, Italy; luca.nodari@cnr.it
3 Department of Engineering "Enzo Ferrari", University of Modena and Reggio Emilia, Via Pietro Vivarelli 10, 41125 Modena, Italy; luca.pasquali@unimore.it (L.P.); magdalena.gualtieri@unimore.it (M.L.G.); miriam.hanuskova@unimore.it (M.H.)
4 Istituto Officina dei Materiali (IOM), The Italian National Research Council (CNR), AREA Science Park, Basovizza, 34149 Trieste, Italy
5 Department of Physics, University of Johannesburg, P.O. Box 524, Johannesburg 2006, South Africa
6 Interdepartmental Research Centre for Applied Research and Services in the Advanced Mechanics and Motor Sector, University of Modena and Reggio Emilia, Via Pietro Vivarelli 2, 41125 Modena, Italy
7 Department of Earth, Environmental and Life Sciences (DISTAV), University of Genoa, 16132 Genoa, Italy; soniascarfi@unige.it (S.S.); serenamira94@gmail.com (S.M.)
8 Inter-University Center for the Promotion of the 3Rs Principles in Teaching & Research (Centro 3R), 56122 Pisa, Italy
9 Department of Physics and Earth Sciences, University of Ferrara, Via Saragat 1, 44122 Ferrara, Italy; tssmrt@unife.it
* Correspondence: dario.digiuseppe@unimore.it; Tel.: +39-0592058497

Abstract: Today, despite considerable efforts undertaken by the scientific community, the mechanisms of carcinogenesis of mineral fibres remain poorly understood. A crucial role in disclosing the mechanisms of action of mineral fibres is played by in vitro and *in vivo* models. Such models require experimental design based on negative and positive controls. Commonly used positive controls are amosite and crocidolite UICC standards, while negative controls have not been identified so far. The extensive characterisation and assessment of toxicity/pathogenicity potential carried out in this work indicate that the commercial fibrous wollastonite NYAD G may be considered as a negative standard control for biological and biomedical tests involving mineral fibres. Preliminary *in vitro* tests suggest that wollastonite NYAD G is not genotoxic. This material is nearly pure and is characterized by very long (46.6 µm), thick (3.74 µm) and non-biodurable fibres with a low content of metals. According to the fibre potential toxicity index (FPTI) model, wollastonite NYAD G is an inert mineral fibre that is expected to exert a low biological response during *in vitro*/*in vivo* testing.

Keywords: fibrous wollastonite; mineral fibres; standard; negative control; FPTI

Citation: Di Giuseppe, D.; Scognamiglio, V.; Malferrari, D.; Nodari, L.; Pasquali, L.; Lassinantti Gualtieri, M.; Scarfì, S.; Mirata, S.; Tessari, U.; Hanuskova, M.; et al. Characterization of Fibrous Wollastonite NYAD G in View of Its Use as Negative Standard for *In Vitro* Toxicity Tests. *Minerals* **2021**, *11*, 1378. https://doi.org/10.3390/min11121378

Academic Editor: Yul Roh

Received: 11 November 2021
Accepted: 2 December 2021
Published: 7 December 2021

1. Introduction

In recent years, awareness of the health risk posed by asbestos has led to a growing interest in the study of mineral fibres [1–10]. Asbestos is a commercial term that designates six mineral fibres (i.e., amosite, asbestos actinolite, asbestos anthophyllite, asbestos tremolite, chrysotile and crocidolite) widely known and used in the past for a huge number of industrial applications but currently classified as carcinogenic to humans by the International Agency for Research on Cancer (IARC) [11]. According to evidence from

epidemiological investigations and laboratory studies [11], the inhalation of airborne asbestos fibres (from occupational or environmental exposure) is associated with an increased risk of developing pulmonary diseases like fibrosis (i.e., asbestosis), pleural abnormalities (effusions and plaques) and malignancies (e.g., lung carcinoma and mesothelioma). Driven by the results of asbestos studies, recent investigations have demonstrated that other mineral fibre species may be responsible for adverse human health effects [12,13]. For instance, lung malignancies development has been observed in populations exposed to fibrous erionite in Turkey [14], fibrous fluoro-edenite in Italy [8,13], fibrous winchite and richterite in the USA [5,9], and fibrous antigorite in New Caledonia [7]. IARC currently classifies the following mineral fibres in Group 1 "Carcinogens for humans": asbestos [11], fibrous erionite [12] and fibrous fluoro-edenite [13]. At the same time, other mineral fibres have been classified in Group 3: fibrous sepiolite [15], fibrous wollastonite [16], fibrous mordenite [17] and short fibres (fibre length < 5 μm) of palygorskite [18]. The Group 3 category concerns agents for which the evidence of carcinogenicity is inadequate for humans and inadequate or limited for animals [19].

Although the aetiology of mineral fibre-related diseases has been the subject of extensive studies [1,14,20–23], the actual mechanisms by which these particles induce adverse effects *in vivo* are not fully understood to date. However, much progress has been made in identifying the properties of mineral fibres that make them cyto-genotoxic agents [24]. One of the most important features is their size. Mineral fibres (especially those with length > 8 μm and width < 0.25 μm) due to their elongated crystal habit cannot be completely engulfed by macrophages whose cell diameter generally ranges from approximately 10 to 20 μm [25–27]. This leads to frustrated phagocytosis, which is characterized by activation of the oxidative burst and release of reactive oxygen (ROS) and nitrogen species (RNS) [28]. Prolonged production of ROS/RNS leads to oxidative stress, chronic inflammation and DNA damage [21,28]. The size of the fibres plays a key role especially in the onset of malignant mesothelioma (MM) [24,25,27]. The small width of the mineral fibres (<3 μm) allows them to reach the pleural cavity [25,27]. The short fibres, with length < 5 μm, leave the pleura through the stomatal openings in the parietal pleura and end up in the lymphatic capillary system [27]. Conversely, stomata are the site of retention of long fibres (>5 μm) which cannot negotiate them [27]. The persistence of the fibres in the pleural space induces chronic inflammation and damage to the mesothelial cells [20,21]. The biopersistence of fibres, defined as their ability to persist in the human body to chemical, physical, and other physiological clearance mechanisms, is another important factor [27,29]. As a matter of fact, to induce chronic inflammation, fibres must persist within the lung tissue and remain chemically and physically unaltered [20,27]. The presence of iron and other metals in the mineral fibres play a key role in the fibre-induced oxidative stress [30]. Available redox-active metals on the fibre surface or released during its partial dissolution promotes the generation of ROS through Haber–Weiss and Fenton reactions [24]. The current knowledge of the physical/chemical and morphological properties of mineral fibres responsible of adverse effect *in vivo* has recently been revised and improved by Gualtieri [24]. Based on these properties, Gualtieri [24] also proposed a quantitative predictive model of potential toxicity/pathogenicity of mineral fibres. This model delivers a fibre potential toxicity index (FPTI) aimed at predicting the toxicity/pathogenicity of minerals fibres [24]. To calculate the FPTI, the model considers all the mineral fibres parameters inducing biochemical mechanisms responsible for *in vivo* adverse effects, i.e., morphometric-, chemical-, biodurability-related, and surface activity-related parameters [24].

Overall, the toxicity mechanism of mineral fibres is linked to several cell-fibre interactions that are regulated by complex cell processes and intercellular relationships investigated through *in vitro* and *in vivo* models [20–23,31–40]. *In vitro* and *in vivo* bioassays provide reliable information on the cellular and tissue response following exposure to hazardous mineral fibre. Bioassays invariably require positive and negative controls in their experimental procedures [41,42]. Basically, positive and negative controls are used as a reference to estimate, by comparison, the *in vitro* or *in vivo* response of the test

substance [41,42]. In toxicity studies, a negative control is a specific substance or sample included in the experimental procedure that is treated in the same way as all other samples but which is not expected to induce toxic effects [41]. The crucial role of a negative control is to avoid non-causal associations between exposures and test results, which can lead to misinterpretation [42]. On the other hand, the positive control sample has an expected toxic effect and will attest that the experimental protocol has been carried out correctly [41]. Consequently, the ideal positive control is a sample that has a predictable toxic and/or pathogenic effect when tested *in vitro* and/or *in vivo* systems, respectively. Currently, amosite (NB #4173-111-4) and crocidolite UICC standards (NB #4173-111-3) are recognized by the scientific community as the most suitable positive reference materials for testing on mineral fibres [31–40]. Conversely, there is no consensus on the standard materials to be used as negative controls. In the few studies on mineral fibres in which a negative control was included in the experimental items, glass beads were mainly used for *in vitro* tests [39,40] and salt solutions or distilled water for *in vivo* tests [32]. However, an ideal negative control should provide a response comparable to that of the test substance [41]. Therefore, the suitable negative control should be a non-toxic mineral fibre. The present work, based on a detailed characterization and evaluation of the sample by the FPTI model, shows that fibrous wollastonite may be used as a reference negative control in biological assays on mineral fibres.

Wollastonite is a single-chain inosilicate, with ideal chemical formula $CaSiO_3$ and a chain repeat unit of three silicon-oxygen tetrahedron $(Si_3O_9)^{6-}$ [43–45]. The chains of tetrahedra are linked to three columns of Ca-centred octahedral or pseudo-octahedral deformed polyhedra [44,45]. Because of the size mismatch of the tetrahedral and octahedral units, the tetrahedra are tilted to accommodate their apices to the apices of the octahedra [44,45]. Tetrahedral chains are organised in pairs composed of inversion-related chains extending along *b*-axis [44,45]. Wollastonite form polytypes that arise through the variation of the unit-cell stacking along the *a*-axis [44,45]. Detailed information on the crystal-chemistry and structural characteristics of wollastonite polytypes can be found in the works of Angel [44] and Mazzucato and Gualtieri [45].

Wollastonite is a ubiquitous mineral and is known to develop crystals with an acicular and/or fibrous crystal habit [43,46]. This morphology confers high strength and makes wollastonite of considerable importance for industrial applications [46]. Wollastonite is extensively used for the production of paint [47], coatings [48], ceramics [49], paper [50], resins [51] and polymers [52]. Due to its chemical stability and thermal resistivity, fibrous wollastonite is used as substitute for asbestos in the manufacture of building material [53]. In addition to its traditional uses, wollastonite has also been used as a bioactive material for biomedical applications [54], soil conditioner for agricultural purposes [55], pollutant absorber for environmental applications [56] and raw material for carbonation reactors used for CO_2 sequestration [57]. The main wollastonite mines are located in China, Finland, India, Mexico, and the USA [46]. According to worldwide mine production data published by the United States Geological Survey (USGS), the global leader in wollastonite production is China with an estimated 890,000 t in 2020. India follows with 120,000 t. Mexico and Canada are in third and fourth place with about 100,000 and 20,000 t, respectively [58]. USA production data missing from USGS reports, but estimated to be substantial and unchanged from 2019 [58].

Because wollastonite used for industrial applications may contain respirable fibres, potential health issues associated with this material have raised general concerns [16,46,53]. A comprehensive review of toxicological and epidemiological data concerning wollastonite can be found in Maxim et al. [46]. As extensively explained in that review, it is not possible to unequivocally exclude that wollastonite is a potential hazard to humans; however, its potential is considered to be low because, as evidenced by *in vivo* tests, wollastonite has a low biopersistence [46,53]. Epidemiological data on wollastonite are limited, but the available data do not suggest that workers exposed to this mineral are at significant risk of an increased incidence of lung cancer or MM [16,46,53]. In Monograph 68, the IARC stated

that there is insufficient evidence in both humans and animals for the carcinogenicity of wollastonite [16].

Our study focused on commercial wollastonite NYAD G from Essex County, New York (USA). The sample was thoroughly characterised using a suite of experimental techniques, to determine morphometric, chemical, biodurability, and surface activity parameters. These parameters were used to calculate the FPTI and assess the potential toxicity/pathogenicity of wollastonite NYAD G. Additionally, to consolidate the results obtained through the FPTI model, an *in vitro* genotoxicity test was performed on wollastonite NYAD G. Specifically, the double-strand DNA breaks induced by wollastonite NYAD G was examined in human monocytic THP-1 cell line by γH2AX assay. Crocidolite UICC standard was tested for comparison.

2. Materials and Methods

2.1. Source of the Sample and Geological Overview

In this study, a commercial sample of wollastonite NYAD G from Willsboro-Lewis mining district (New York, NY, USA) in the eastern Adirondack Mountains, has been investigated. Wollastonite NYAD G is produced by NYCO Minerals Inc., a subsidiary of Imerys. NYCO Minerals is the leading North American supplier of wollastonite and its mining production covers large part of the global demand for wollastonite [59]. Wollastonite NYAD G is a raw material commonly used as a reinforcing and thermal insulating agent for the production of protective coatings.

A complete and accurate description of the geological features of the Willsboro-Lewis mining district and geodynamic processes that characterized the tectonics of this area can be found in Whitney and Olmsted [60] and Peck and Bailey [61]. Briefly, Willsboro-Lewis mining district is a mixed zone made up of mafic (anorthositic to gabbroic) gneiss, granitic gneiss, amphibolite, quartzite, pelite, calc-silicate, marble, and skarn. The ore zone is characterized by layers containing wollastonite, garnet (grossular-andradite mixtures) and clinopyroxene, produced by hydrothermal metasomatism. Before being marketed, wollastonite undergoes various industrial treatments to remove impurities [53].

2.2. X-ray Powder Diffraction (XRPD)

XRPD data were collected using a conventional Bragg–Brentano Philips diffractometer (model PW-1729), with θ–2θ geometry, Cu$K\alpha$ radiation, 40 kV, 30 mA and gas-filled proportional detector (Malvern Panalytical, Malvern, UK).

The sample is supplied in powder form, so it does not need to be milled before running the analysis. Wollastonite powder was mounted in sample holders using a side-loading technique. A step scan of 0.02 °2θ was used with a time of 3 s/step in the 5–65° 2θ range. The incident beam pathway included: 1/2° divergence slit, 1/2° anti-scattering slit. The XRPD pattern of wollastonite NYAD G was analysed using the X-Pert High Score Plus suite [62].

2.3. Thermogravimetric Measurements and Analysis of the Evolved Gases with Mass Spectrometry

Thermogravimetric (TG) analyses were performed with the thermal analyser Seiko SSC 5200 (Seiko Instruments Inc., Chiba, Japan) paired with a quadrupole mass spectrometer (ESS, GeneSys Quadstar 422) to analyse gases released during thermal reactions (MSEGA) (ESS Ltd, Cheshire, UK) mpling is through an inert, fused silicon capillary system, heated to prevent condensation. The intensity of the signal of selected target gasses were collected in multiple ion detection mode (MID) using a secondary electron multiplier operating at 900 V. More specifically, we measured the intensity of the signals of the m/z ratios 18 for H_2O, 30 for NO, 44 for CO_2, 64 for SO_2, where m/z is the ratio between the mass number and the charge of the ion. The heating condition were 20 °C/min in the thermal range 25–1000 °C using ultrapure helium at a flow rate of 100 μL/min as purging gas.

2.4. Scanning Electron Microscopy

Morphometric investigation of wollastonite NYAD G was performed using a JSM-6010PLUS/LA (JEOL Ltd., Musashino, Japan) scanning electron microscope (SEM) equipped with an energy-dispersive X-ray (EDX) spectrometer (Oxford INCA-350) (Oxford Instruments, Abingdon-on-Thames, UK). The sample was prepared as follows: some milligrams of the sample were suspended in 5 mL of water and a drop of the suspension was placed on conductive double-stick carbon tape attached to an aluminium stub. After complete evaporation of the water, the sample was coated with a thin film of carbon (10 nm thick) using a Carbon Coater-Balzers CED-010. A series of representative SEM images were analysed using ImageJ software, which provides accurate measurements of fibre length and width [63].

2.5. Determination of the Specific Surface Area

Specific surface area (SSA) of the sample was determined using the BET-method [64]. The SSA analyses were carried out using a Gemini V Micromeritics instrument (Micromeritics Instrument Corp., Norcross, GA, USA) [65], with nitrogen as probe gas. About 300 mg of sample dehydrated at 100 °C for 24 h was mounted in the sample holder and conditioned at 50 °C prior to measurement. The analysis was carried out at the temperature of −196 °C. Measurements were conducted with an equilibration time of 10 s and the saturation pressure of 777.280 mmHg.

2.6. Determination of the Density

Density (ρ) of the sample was measured using a gas pycnometer AccuPyc II 1340 Micromeritics (Micromeritics Instrument Corp., Norcross, GA, USA) [65]. Helium with a total purity > 99.999% mol was used as dispersion medium.

2.7. Determination of the Zeta Potential

The zeta potential of the sample was determined using a Zetasizer Nano Series Malvern instrument. Analyses (Malvern Panalytical, Malvern, UK) were performed using double-distilled water and artificial lysosomal fluid (ALF) solution (pH = 4) [65,66]. The latter was used to simulate the lysosomal environment [66]. Sample powder was added to the dispersants in a weight percentage of 0.1% and subjected to ultrasonic treatment for 15 min. Zeta potential measurements were conducted at a temperature of 37 °C, equilibration time of 120 s and different pH (from 2 to 11). A few drops of HCl 1N were added to the suspension to obtain a pH of 2. The pH was then raised up to 11 using NaOH 0.1 N. The pH was monitored using a HANNA edge pH-meter. Zeta potential measurements were collected three times for each sample to check the reproducibility of the results.

2.8. Electron Probe Micro Analysis (EPMA)

Quantitative chemical composition of the wollastonite NYAD G fibres was obtained using a JEOL 8200 SuperProbe Electron Probe Microanalyzer (JEOL Ltd., Musashino, Japan) equipped with a Wavelength-Dispersive X-ray (WDS) spectrometer system and W hairpin type filament. Detectable wavelength is 0.087 to 9.3 nm. Atomic number resolution on BSE (Z): less/equal than 0.1 (CuZ). The following analytical conditions were used: excitation voltage of 15 kV, specimen current of 5 nA, peak-count time of 30 s, background-count time of 10 s. The instrument is also equipped with an EDX system characterized by a detectable element range: Na to U, energy resolution: 144 eV and lithium (Li)-doped silicon single-crystal semiconductor detector. Before we carried out the analysis, an aliquot of the sample was embedded in epoxy resin (shaped into a disc with a diameter of 25 mm), then polished to achieve a flat, shiny, surface [65]. The following elements were determined for each spot analysis (detection limits are indicated in brackets): Al (0.04 wt%), Ca (0.02 wt%), Fe (0.04 wt%), K (0.01 wt%), Mg (0.03 wt%), Mn (0.04 wt%), Na (0.03 wt%), Si (0.04 wt%), Ti (0.03 wt%), Ni (0.05 wt%), Cr (0.04 wt%), Pb (0.06 wt%), V (0.10 wt%), Co (0.04 wt%), Cu

(0.05 wt%), Zn (0.07 wt%), Sb (0.08 wt%), As (0.14 wt%), Hg (0.09 wt%) and Cd (0.04 wt%). The standards utilized were: mono-elemental standard for V, Cr, Co, Cu, Cd, Sb and Zn; nickeline for Ni and As; galena for Pb; omphacite for Na; orthoclase for K; mercuric sulfide for Hg; rhodonite for Mn; forsterite for Mg; fayalite for Fe; ilmenite for Ti; grossular garnet for Al, Si and Ca.

2.9. Mössbauer Spectroscopy

Room temperature Mössbauer spectra were collected at the Department of Chemical Science (University of Padova), by means of a conventional constant acceleration spectrometer mounting an ^{57}Co source, nominal strength 1850 MBq. The sample was prepared by mixing ≈ 70 mg of wollastonite, gently crushed in acetone, with Vaseline. The thin absorber thickness was checked according with [67] and the effect of thickness considered inappreciable. The spectrum was fitted to Lorentzian line shapes with the minimum number of components, by using Recoil software [68]. The hyperfine parameters isomer shift (δ), quadrupole splitting (Δ), half linewidth at half maximum (Γ_+) were expressed in mms^{-1}, while the relative area (A) in %.

2.10. X-ray Photoelectron Spectroscopy (XPS)

XPS measurements were taken to reveal the Fe^{2+}/Fe^{3+} ratio at the close-to-surface layers of wollastonite fibres. XPS spectra were acquired with an OMICRON EA125 electron hemispherical analyser (Omicron NanoTechnology, Taunusstein, Germany) operated at 25 eV of pass energy at normal emission and a double anode XR3 VG source, delivering Mg Kα photons (1253.6 eV), at 15 kV, 18 mA.

2.11. Ultraviolet-Visible (UV-Vis) Spectroscopy

An UV-Vis spectrum of wollastonite NYAD G was collected in diffuse reflection using a JASCO model V-570 UV/VIS/NIR spectrometer equipped with a 60 mm integrating sphere (Jasco ISN-470) and PSH-001 powder sample holder (JASCO Corp., Tokyo, Japan). UV-Vis adsorptions were recorded at room temperature with scanning speed 1000 nm/min and converted into the Kubelka–Munk function [69]. Deconvolution of the spectrum was performed with the PeakFit 4.12 software (Systat Software Inc., San Jose, CA, USA) [70].

2.12. Biodurability

Biodurability of the sample was evaluated by *in vitro* acellular dissolutions tests in batch reactors at 37 °C [29,65]. Batch leaching tests were conducted using 25 mg of sample and 250 mL of ALF solution at pH = 4.5 [65]. The degree of dissolution was determined by measuring the change of the sample mass after different times: 24 h, 48 h, 1 week, 2 weeks, 1 month, 2 months and 3 months [65]. A detailed description of the procedure used for the analysis of dissolution data and determination of kinetic parameters can be found in Gualtieri et al. [71].

2.13. Determination of the Fibre Potential Toxicity Index (FPTI) of Wollastonite

To calculate the FPTI of a mineral fibre, the model considers morphometric, chemical, biodurability related, and surface parameters of mineral fibres that affect their toxicity and pathogenicity upon inhalation [24]. Table 1 summarizes the parameters of the model used for the calculation of the FPTI of wollastonite NYAD G.

Table 1. The parameters used and the calculated fibre potential toxicity index (FPTI) for the fibrous wollastonite NYAD G (New York, USA). For comparison, the values calculated for fibrous wollastonite NYAD G staring form literature data [24], asbestos tremolite from Val d'Ala (Italy) [24] and chrysotile from Balangero (Italy) [65] are reported.

Parameters	Classes	Normalized Score $FPTI_i$	Chrysotile, Balangero [65]	Asbestos Tremolite, Val D'Ala [24]	Wollastonite NYAD G [24]	Wollastonite NYAD G [This Study]
Length	>5 μm and <10 μm	0.10	0.40	0.40	0.20	0.40
	>10 μm and <20 μm	0.20				
	>20 μm	0.40				
Diameter	>1 μm and <3 μm	0.10	0.10	0.10	0.10	0.00
	>0.25 μm and <1μm	0.20				
	<0.25 μm	0.40				
Crystal curvature	Flat surface	0.05	0.20	0.05	0.05	0.05
	Altered surface	0.10				
	Cylindrical surface	0.20				
Crystal habit	Curled	0.10	0.10	0.40	0.40	0.40
	Mixed curled/acicular	0.20				
	Acicular	0.40				
Fibre density	<2.75 g/cm^3	0.05	0.05	0.10	0.10	0.10
	>2.75 and <3.5 g/cm^3	0.10				
	>3.5 g/cm^3	0.20				
Hydrophobic character of the surface	Hydrophobic	0.05	0.20	0.20	0.20	0.20
	Amphiphilic	0.10				
	Hydrophilic	0.20				
Surface area	>25 m^2/g	0.05	0.05	0.20	0.20	0.20
	<25 and >5 m^2/g	0.10				
	<5 m^2/g	0.20				
Total iron content	Fe_2O_3 + FeO wt% < 1	0.05	0.10	0.10	0.05	0.05
	1 < Fe_2O_3+FeO wt% < 10	0.10				
	Fe_2O_3 + FeO wt% > 10	0.20				
Ferrous iron	0 < FeO wt% < 0.25	0.05	0.20	0.20	0.05	0.10
	0.25 < FeO wt% < 1	0.10				
	FeO wt% > 1	0.20				
Surface ferrous iron/iron nuclearity	Fe^{2+} nuclearity > 2	0.02	0.033	0.033	0.02	0.067
	Fe^{2+} nuclearity = 2	0.033				
	Fe^{2+} nuclearity = 1	0.067				
Content of metals other than iron *	$\sum_i \frac{C_i}{L_i} < 1$	0.10	0.40	0.40	0.10	0.10
	$1 < \sum_i \frac{C_i}{L_i} < 5$	0.20				
	$\sum_i \frac{C_i}{L_i} > 5$	0.40				
Dissolution rate log(R) **	<1 y	0.05	0.05	0.20	0.05	0.05
	>1 and <40 y	0.10				
	>40 y	0.20				
Velocity of iron release ***	<0.1	0.033	0.133	0.067	0.033	0.067
	>0.1 and <1	0.067				
	>1	0.133				
Velocity of silica dissolution ****	<0.5	0.02	0.067	0.033	0.067	0.067
	>0.5 and <1	0.033				
	>1	0.067				
Velocity of release of metals *****	<1	0.033	0.133	0.133	0.067	0.033
	>1 and <10	0.067				
	>10	0.133				
Zeta potential	Negative at pH = 4.5	0.10	0.10	0.20	0.20	0.20
	Negative at both pH = 4.5 and 7	0.20				
Fibres' aggregation	Zeta potential > |20|	0.033	0.033	0.067	0.033	0.033
	|10| < Zeta potential < |20| |0| < Zeta potential < |10|	0.067 0.133				
Cation exchange (in zeolites)	Cation Exchange	0.067	0.00	0.00	0.00	0.00
	No cation exchange	0.00				
FPTI (error)			2.35(0.22)	2.88(0.43)	1.92(0.30)	2.12(0.18)

* detailed description of the parameter "non-iron metal content" is given in reference [24]; ** the total dissolution time of the fibre calculated in years (y) [71]); *** total content of elemental iron in the fibre (wt%) possibly made available as active iron at the surface of the fibre divided by the total dissolution time (y) of the fibre; **** total content of Si of the fibre (wt%) divided by the total dissolution time (y) of the fibre; ***** total content (ppm) of heavy metals (Sb, As, Hg, Cd, Co, Cr, Cu, Pb, Ni, Zn, V, Be; Mn, Be) divided by the total dissolution time (y) of the fibre.

The length and width of mineral fibres are key factors in mineral fibre-induced frustrated phagocytosis and inflammation process [24,25,27]; while the curvature of the surface of the fibres plays a role in the proteins binding process and influence cell adhesion [24]. The crystal habit and density of a fibre influences its depositional pathway in the respiratory tract [24]. The surface area (expressed as BET-SSA) is a parameter that affects the biodurability and biopersistence of mineral fibres [24,71]. SSA directly influences the dissolution rate of a fibre and is included as a factor in the equation used to determine its apparent dissolution rate (R) [24,71]. A larger surface area determines a higher reactivity of the mineral fibres in solution. In acidic environment (as the one found in lung tissue) particles with large surface area (e.g., chrysotile fibres) are more reactive than those with low surface area (e.g., tremolite fibres) [24,71]. The hydrophobic character of a fibre rules the interaction with biopolymers and phagocytic cells [24]. Iron of mineral fibres promotes the formation of ROS and RNS [24]. The main role in the catalysis of the reductive oxide processes associated with the production of ROS/RNS is played by Fe^{2+} [24]. Reactivity of iron is related to its nuclearity (i.e., number of iron atoms joined in single coordination entity by bridging ligands) [24]. The content of potential toxic metals is important as these elements are capable of induction inflammation activity *in vivo* [24,29]. Dissolution rate is the key parameter of fibre biodurability [71]. A fibre with a high dissolution rate is assumed to have a low biodurability and in principle is less toxic than a fibre with high biodurability [24,71]. The rate of dissolution of iron, silica and metals controls the release into the extracellular space of substances that may generate ROS and RNS [24,29,71]. The zeta potential quantitatively assesses the electrical charges surrounding the fibres. This parameter may affect the haemolytic activity, ROS production, fibre encapsulation, apoptosis and fibre's aggregation [24]. The cation exchange capacity is a property of fibrous zeolites like erionite. Zeolites can release or exchange cations in an organic medium such as the cytoplasm and interfere with cell cycles [24].

For each parameter, a score is assigned depending on its measured value and its supposed capability in inducing adverse effects (Table 1). Because the parameters of the model can be correlated with each other, a hierarchical scheme considering the cross-correlations is applied [24,72]. A weighing scheme is associated with each parameter of the model according to its step/hierarchy H where $w_1 = 1/H$ with H = 1, 2 or 3. A weight defined as $w_2 = 1/U$ is also applied to each parameter of the model. It accounts for the uncertainty in the determination of a specific parameter (n, m) and is defined by the penalty parameter U (1 = low to null uncertainty, 2 = some degree of uncertainty, 3 = high uncertainty). Having defined the weighing scheme of the parameters, the FPTIi is calculated according to Equation [24]:

$$FPTI_i = \sum_{i=1}^{n} w_1 \cdot w_2 \cdot T_i$$

with T_i = class value of the parameter i of the model; $w_1 = 1/H$ weight of the parameter according to its hierarchy H; $w_2 = 1/U$ weight of the parameter according to the uncertainty U of its determination.

2.14. In Vitro DNA Damage Quantification

The human monocytic cell line THP-1 was obtained from the American Type Culture Collection (LGC Standards srl, Milan, Italy). Cells were cultured at 37 °C in a humidified, 5% CO_2 atmosphere in RPMI-1640 with L-glutamine 2 mM (Euroclone, Milan, Italy), supplemented with 10% FBS (Euroclone), 50 µM β-mercaptoethanol and penicillin/streptomycin as antibiotics (Corning Inc., Corning, NY, USA).

The presence of double-strand breaks in the DNA of THP-1 monocytic cell line were analysed by evaluating nuclear γH2AX histone foci [73]. THP-1 monocytes were seeded in eight-well Lab-Teck chambered slides at 75,000 cells/well in complete medium and the day after they were induced to polarize to M0 macrophages by adding 20 ng/mL phorbol-12-myristate 13-acetate (PMA, PeproTech EC, London, UK) to the culture medium for 48 h.

Subsequently, non-adherent cells were removed and M0 macrophages and incubated or not (control) with 50 μg/mL of crocidolite UICC or wollastonite NYAD G. After 24 h, cells were stained with anti-γ H2AX antibody (Abcam), while the nucleus was coloured with 2 μg/mL propidium iodide. Images were acquired with a Leica TCS SL confocal microscope with an HCX PL APO CS 63.0 × 1.40 oil objective. The nuclei images (4.0 × digital zoom) were acquired with the fluorescent foci of double-strand breaks in the DNA in green and the propidium iodide-positive nuclei in red (excitation at 488 nm for both and emission range of 500–550 nm and 600–670 nm, respectively).

3. Results

3.1. Characteristics of Wollastonite NYAD G

Wollastonite occurs in nature in association with other mineral phases, some of which can be potential toxic contaminants, e.g., crystalline silica and asbestos [53]. The sample characterisation carried out in this work has unequivocally demonstrated that there is no contamination with asbestos or other hazardous phases in the wollastonite NYAD G sample.

The XRPD pattern (5–65 °2θ) of the sample is shown in Figure 1a. The qualitative mineralogical analysis showed that wollastonite NYAD G mainly contains wollastonite-1A polytype. As shown in Figure 1b, all peak positions in the sample XRPD pattern match those associated with wollastonite-1A (JCPDS card 01-073-1110). The presence of calcite in the sample was evidenced by TG analysis (Figure 2). The thermogravimetric analyses and its first derivative (DTG) curves (Figure 2a) showed one main thermal event between 535 and 765 °C with maximum reaction rate at 650 °C and a mass loss of 0.44 wt%. The MSEGA curves (Figure 2b) clearly evidenced the release of CO_2 (m/z = 44) in the same thermal range, suggesting that the reaction is due to decarbonation. The mass loss which occurs before this reaction is essentially due to the removal of physio adsorbed water (mass loss of about 0.3 wt% between 25 and 535 °C), as mirrored by the almost analogue variation of the intensity of the signal related to water (m/z = 18, Figure 2b). No reaction associated with NO and/or SO_2 was observed. Decarbonation reactions can occur at varying temperature values (usually between 550 and 850 °C) depending on both the cation and the overall sample characteristics, such as the occurrence of other phases, genetic conditions, degree of alteration, etc. [74]. Wollastonite forms essentially by thermal metamorphism of rocks containing silicates and calcium carbonate. Therefore, although the XRPD pattern does not shows peaks unequivocally related to calcium carbonate, it is likely that the decarbonation is due to thermal decomposition of calcite, although the pure term should decompose at significantly higher temperature (about 780 °C). From the associated mass loss, it can be calculated that the amount of calcite in the sample is approximately 1.0 wt%.

Figure 3 shows a selection of SEM images and an EDX spot analysis of the sample. Wollastonite NYAD G consists of long thick fibres with a low degree of flexibility. The fibres display a flat surface, regular terminations and a straight shape. The summary statistics of the morphometry of the wollastonite fibres are reported in Table 2. The data show a wide range of lengths, with values ranging from 8.17 to 228 μm, but long fibres predominate in the population (Table 2). In fact, more than 75% of wollastonite fibres are longer than 21.5 μm. The average length (L) of wollastonite NYAD G fibres is 46.6 μm. The width (W) of the fibres range overall between 1.09 and 18.1 μm, but 75% of the fibres display a width of greater than 2.42 μm (Table 2). The average fibre width is 3.74 μm. All of the fibres have an aspect ratio (L/W) > 4:1 (average 13). The relationship between fibre size and carcinogenicity has been widely discussed in the literature [24,25,27]. However, it is commonly recognised that respirable size fibres with relevant biological activity are those longer than 5 μm, with widths of less than 3 μm and with an aspect ratio of >3:1 [24,72,75]. Although all of the observed wollastonite fibres meet the length and aspect ratio criteria, 50% of them do not have the ideal W to be defined regulated mineral fibres (Table 2) [75]. Typical EDX spectrum of wollastonite NYAD G is shown in Figure 3d. Qualitative analysis of the spectrum showed that the sample is composed mainly of Si and

Ca. SEM-EDX analysis revealed the presence of isolated calcite crystals within the sample. A representative image of the calcite is shown in Figure S1 deposited in the Supplementary Materials together with the EDX spectrum that enabled its recognition.

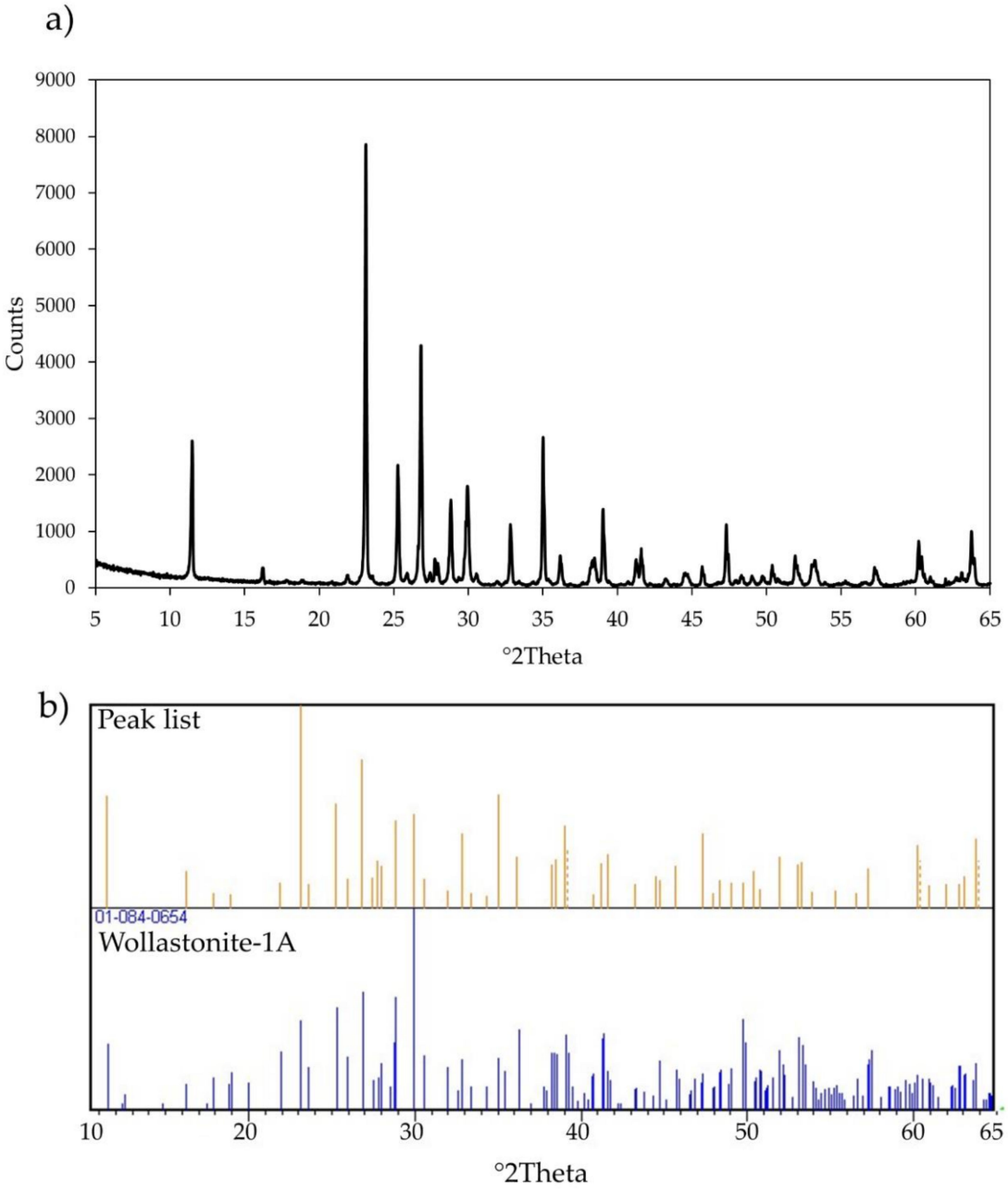

Figure 1. (**a**) X-ray diffraction pattern of wollastonite NYAD G. (**b**) Comparison of diffraction peaks of wollastonite NYAD G with the diagnostic peaks of wollastonite-1A (JCPDS card 01-073-1110).

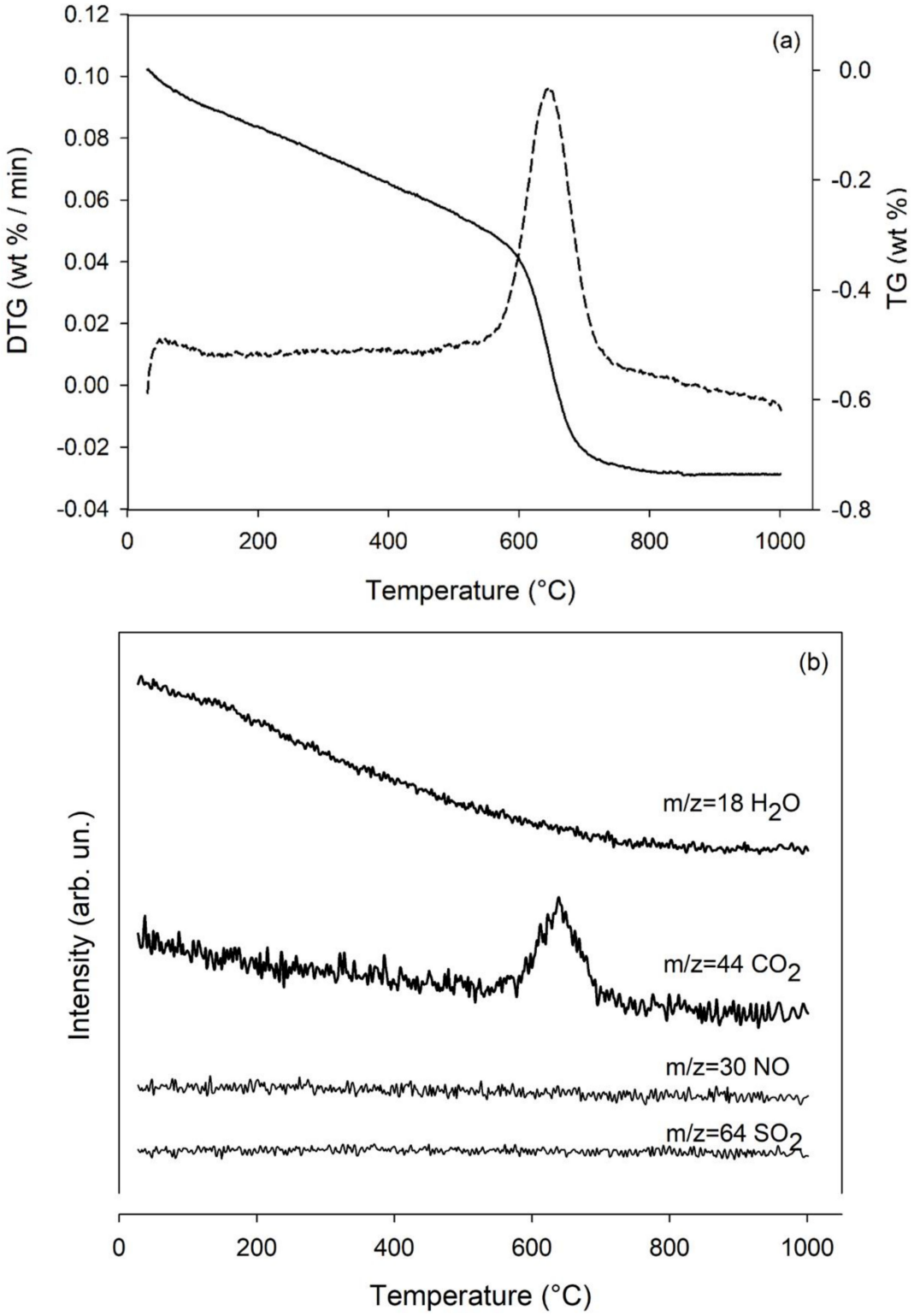

Figure 2. (**a**) Thermal analyses (TG, solid line) and first derivative (DTG, dashed line) curves of the wollastonite NYAD G. (**b**) Evolved gas mass spectrometry (MS-EGA) of the sample. arb. un. (arbitrary units).

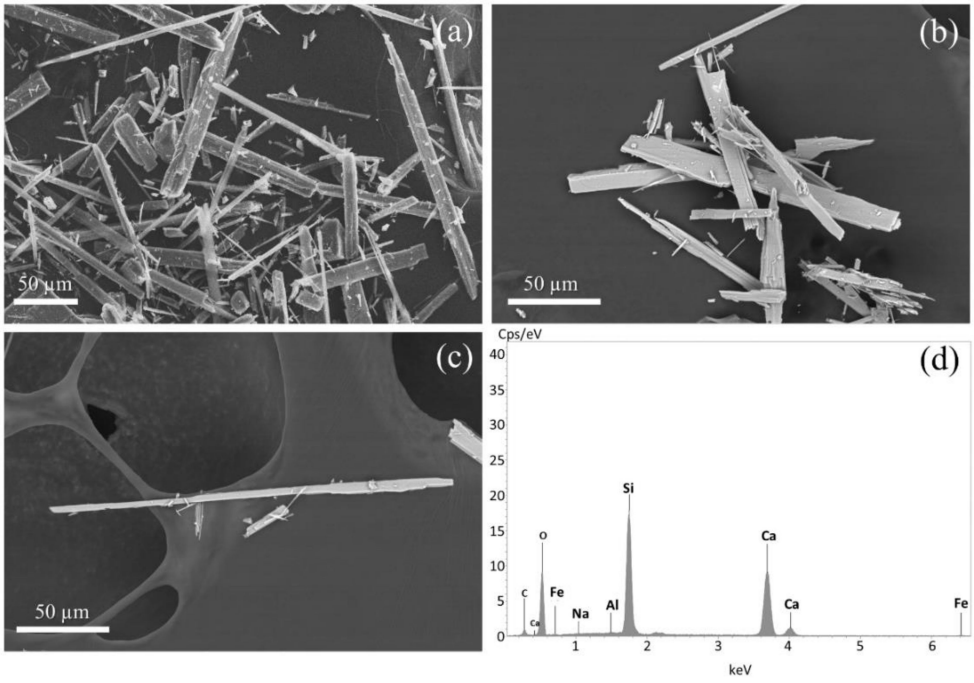

Figure 3. Representative scanning electron microscopy (SEM) images (**a**–**c**) and energy-dispersive X-ray (EDX) spectrum (**d**) of wollastonite NYAD G fibres. (**a**,**b**) SEM images show that the sample consists of elongated particles of different sizes. (**c**) Single acicular fibre with flat surface, parallel sides, regular terminations and a straight shape. (**d**) Typical EDX spectrum of wollastonite. Qualitative analysis shows that the sample is composed mainly of Si and Ca. Traces of Na, Fe and Al also occur.

Table 2. Summary statistic of wollastonite fibres geometry (n = 200). L (length); W (width); Min (minimum); Max (maximum); σ (standard deviation).

	Percentiles *								
	Min	**5th**	**25th**	**50th**	**75th**	**95th**	**Max**	**Average**	**σ**
L (µm)	8.17	13.6	21.5	32.7	57.4	132	228	46.6	38.1
W (µm)	1.09	1.40	2.42	3.17	4.46	7.20	18.1	3.74	2.29

* Percentile indicates the minimum value below which a given percentage of the other elements under observation falls. Example: 25th percentile states that the 25% of fibres have L $\leq$ 25.1 µm and W $\leq$ 2.42 µm.

The density (ρ) of wollastonite NYAD G is 2.98(0.003) g/cm^3 a value that agrees with those reported in the literature, i.e., 2.86–3.09 g/cm^3 [76].

SSA of the wollastonite NYAD G is 0.50 ± 0.01 m^2/g. Compared to other mineral fibres [71], wollastonite has a very low SSA (Table 3). SSA of the fibrous wollastonite is about 20 times lower than amosite and fibrous tremolite and 30 times lower than crocidolite. Chrysotile is the mineral fibre with the absolute highest SSA (Table 3).

Table 3. Kinetic parameters calculated for the dissolution of wollastonite NYAD G and other mineral fibres [71]. Table contains the specific surface area (SSA), apparent rate constant (k), the apparent dissolution rate (R), and the calculated dissolution time for a 0.25 µm tick fibre (t).

	SSA (m^2g^{-1})	**k (s^{-1})**	**R ($mol \cdot m^{-2}s^{-1}$)**	**t(d)**	**t (y)**
Wollastonite NYAD G	0.50(0.01)	$1.98(3) \times 10^{-6}$	$1.59(3) \times 10^{-4}$	30 (15)	0.08 (4)
Balangero chrysotile	42.0(1)	$1.8(6) \times 10^{-10}$	$1.7(6) \times 10^{-10}$	124 (41)	0.3 (1)
UICC amosite	9.5(3)	$6.1(6) \times 10^{-14}$	$2.7(3) \times 10^{-13}$	27,010 (2647)	74 (7)
UICC anthophyllite asbestos	4.4(2)	$1.2(3) \times 10^{-13}$	$1.0(3) \times 10^{-13}$	83,950 (20,990)	245 (64)
Val d'Ala tremolite asbestos	9.2(3)	$5.4(9) \times 10^{-14}$	$4.5(7) \times 10^{-13}$	17,885 (2981)	49.0 (8)
UICC crocidolite	16.1(6)	$1.3(3) \times 10^{-13}$	$3.2(7) \times 10^{-13}$	24,090 (5840)	66.0 (16)

Hydrophobicity and hydrophilicity are properties related to the surface characteristics of the fibres [25,77–80]. Non-polar minerals are hydrophobic, while polar minerals such as silicates (except talc) are hydrophilic [77,78]. Natural wollastonite is a well-known hydrophilic mineral [77,79,80]. Because wollastonite NYAD G is a raw material with preserved natural surface characteristic, we can assume that it possesses a hydrophilic character.

Results of the zeta potential analyses as a function of pH are illustrated in Figure 4. Overall, when the pH of the suspension increases, the zeta potential decreases in both double-distilled water and ALF solution (Figure 4). In the pH range between 2 and 11, the zeta potential of the sample varies from −0.3 to −39 mV in double-distilled water, and ranges from 1.6 to −28 mV in ALF solution.

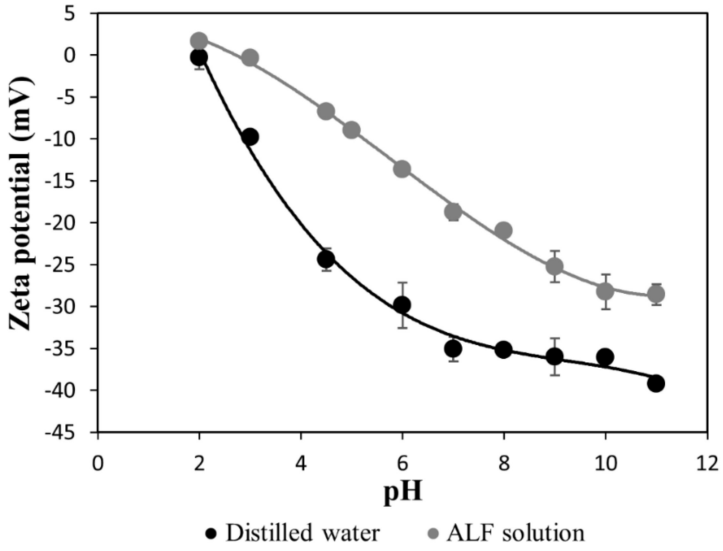

Figure 4. Zeta potential versus pH curves. Black line: wollastonite NYAD G in double-distilled water. Grey line: wollastonite NYAD G in ALF solution.

Representative EMPA element composition of wollastonite NYAD G expressed in weight percent (wt%) with relative standard deviations are reported in the Table 4. The chemical formula of wollastonite NYAD G, as determined from 63 EMPA spot analyses (Table S1 in Supplementary Materials), is:

$$Ca_{0.997}Fe^{2+}_{0.0053}Fe^{3+}_{0.0024}Mn_{0.0025}Mg_{0.0009}Si_{0.9786}O_3$$

Overall, wollastonite NYAD G has a relatively low total iron (Fe_2O_3 + FeO wt% <1) and ferrous (0.25 < FeO wt% < 1) content (Table 4). The Mössbauer spectrum of the wollastonite sample (Figure S2 in Supplementary Materials) shows, despite the high counts ($\approx 13 \times 10^6$), weak signals attributable to both Fe^{3+} and Fe^{2+} moieties. The best tentative of fitting concerns in three doublets: one ascribed to Fe^{3+} (Db1) and two to Fe^{2+} (Db2 and Db3). Both ferrous and ferric species show hyperfine parameters typical of a distorted octahedral environment (Table 5). The Fe^{2+}/Fe^{3+} ratio, calculated considering the relative area (A) of the deconvoluted Fe^{2+} and Fe^{3+} spectral signatures, is 2.2 (Table 5). Wollastonite's structure contains three distinct *M* sites (i.e., *M*1, *M*2 and *M*3) which are usually occupied by Ca [81]. However, both Fe^{2+} and Fe^{3+} can replace Ca as an octahedral cation. According to Ohashi and Finger [82], Fe atoms can occupy all three octahedral sites of wollastonite, but, Mössbauer studies of synthetic and natural iron-wollastonite showed that Fe^{2+} preferentially occupies *M*1 and *M*3 sites [83]. In addition, following the work of Matsueda [83] it is possible to assign the *M*3 site to the outer Fe^{2+} doublet (Db2) and *M*1 site to the inner Fe^{2+} doublet (Db3). Ferric doublet Db1 suggest that Fe^{3+} is located at one of the *M*1-*M*3 sites, however,

the presence of a small amount of Fe^{3+} in the tetrahedral sites as a result of Si^{4+} substitution cannot be excluded.

Results of XPS analyses are shown in Figure S3 deposited in the Supplementary Materials. Supplementary Figure S3 shows the Fe 2p region of the XPS spectrum, after removal of the X-ray satellite lines from photoelectron spectra excited with Mg Kα radiation. The spectrum has been decomposed into Voigt doublets, taking onto account the spin-orbit splitting of Fe $2p_{3/2}$ and $2p_{1/2}$ components, over a Shirley-type background. The spectrum presents characteristic Fe^{2+} and Fe^{3+} main components, accompanied by related satellites. The branching ratio between Fe^{2+}/Fe^{3+} $2p_{3/2}$ components is 1.1.

XPS analysis showed that both Fe^{2+} and Fe^{3+} sites are available at the surface of the wollastonite fibres. However, in order to calculate the FPTI of the sample, it is necessary to know the nuclearity of these Fe^{x+} sites (Table 1). Identifying the nuclearity of Fe^{x+} exposed on the surface of the mineral fibres is very complex and to date the ideal analytical technique for this purpose has not yet been identified. Our research group is currently evaluating various methodologies, and those that seem most promising are: (1) Fourier transform infrared (FTIR) spectroscopy using NO as a probe molecule. The adsorption of NO on the fibre surface leads to the formation of the nitrosyl complex $Fe^{x+}(NO)_n$ characterised by extremely intense υ(NO) bands which are strongly influenced by the Fe oxidation state and nuclearity. This methodology was effectively employed by other authors [84] for the study of the nuclearity of Fe^{x+} active sites in Fe-doped zeolites. (2) UV-Vis spectroscopy. UV-Vis spectra (200–800 nm) contain accurate information about the oxidation and coordination states of metal ions that comes from electronic transitions [69,70]. This technique has been successfully used in the past (see for example [70]) for the qualitative and semi-quantitative evaluation of the nuclearity of the iron species of a synthetic chrysotile. Method (2) is undoubtedly the most accessible, but it fails to discern between surface and bulk Fe^{x+} sites. By contrast, Method (1) offers the best performance in terms of surface sensibility but requires elaborate measurements and the implementation of customised FTIR systems [84]. In the present study, UV-Vis spectroscopy was chosen to preliminary investigate the nuclearity of Fe in wollastonite NYAD G. Given the limitations of Method (2), we are aware that the nuclearity value obtained is mainly representative of bulk Fe. In order to address the issues described above, work is in progress to deliver a quantitative model for the determination of the nuclearity of surface Fe in mineral fibres using Method (1).

Supplementary Figure S4 shows the UV-Vis spectrum of the sample in the region from 200 to 500 nm (no absorption band was detected above 500 nm) deconvoluted into Gaussian sub-bands ($r^2 = 0.981$). Major contributions of the spectrum stem from three short wavelength sub-bands at 218 nm (G1), 254 nm (G2) and 290 nm (G3). The sub-bands at 254 nm and 290 nm are associated with isolated mononuclear Fe located at octahedral *M* sites [69,70]. While the 218 nm band is indicative of the presence of isolated iron sites in tetrahedral coordination [69,70]. Bands between 300–500 (G4 and G5) suggest the presence of octahedral Fe in cluster-like Fe_xO_y species [70]. Since the UV-Vis spectrum shows bands indicative of isolated Fe species, we assume that the nuclearity of Fe is mostly 1.

EMPA spot analyses showed that NYAD G wollastonite does not contain relevant amounts of metals considered as environmental and health hazards (i.e., As, Co, Cr, Cd, Sb, Hg, Cu, Pb, Ni, Zn and V).

Table 3 reports the dissolution kinetic parameters calculated for the dissolution of wollastonite NYAD G. The parameters for other mineral fibres are provided for sake of comparison. The plot of the wollastonite mass loss (%) vs. time (d) is reported in Figure S5 in the Supplementary Materials. The fit of the mass vs time plot allowed to extrapolate the total dissolution time (Figure S5), which is estimated to be t_d = 383(190) d. That time was used to empirically calculate the apparent dissolution rate (R) from the equation modified after Gualtieri et al. [71]:

$$R = \frac{3w}{4Vt_d}$$

where w = mean fibre width (3.17×10^{-6} m), V = molar volume (0.39×10^{-4} m^3/mol) and t_d = total dissolution time [85].

The apparent rate constant (k) is then calculated from the equation modified after Gualtieri et al. [71]:

$$k = R \cdot SSA \cdot m$$

with SSA determined using the BET-method (m^2g^{-1}), m = initial mass of the sample (g). The calculated values are $k = 1.98 \times 10^{-6}$ s^{-1} and $R = 1.59 \times 10^{-4}$ $mol \cdot m^{-2}s^{-1}$. The calculated k value matches with the k values estimated by Rimstidt and Dove [86] during acid dissolution tests of wollastonite from New Mexico. To compare the dissolution kinetics of wollastonite with other relevant mineral fibres, Table 3 shows the calculated dissolution time (t) for a wollastonite fibre with w = 0.25 µm. This value is estimated using the following equation:

$$t = \frac{3w}{4VR}$$

Table 4. Mean values of the EMPA analyses of the wollastonite NYAD G; standard deviation is shown in brackets. The chemical composition of wollastonite NYAD G given in the technical data sheet (TDS) provided by NYCO Minerals Inc. is shown for comparison [87]. Wt% (weight percent); Data from EMPA analyses are replotted considering the value of the L.o.I. (loss on ignition); * bdl (below the detection limit). ** L.o.I. = H_2O wt% determined from TG data. The FeO and Fe_2O_3 concentration was calculated using the stoichiometric criteria of the Droop method [88] and the results of Mössbauer analyses.

Wt%	EMPA	TDS NYCO Minerals
SiO_2	50.76 (0.25)	51.60
FeO	0.33 (0.09)	-
Fe_2O_3	0.17 (0.09)	0.77
MnO	0.15 (0.04)	0.15
MgO	0.03 (0.02)	0.15
CaO	48.27 (0.24)	46.36
Na_2O	* bdl	-
Al_2O_3	bdl	0.40
K_2O	bdl	0.02
TiO_2	bdl	0.05
L.o.I.	** 0.30	0.50
Tot	100.0	100.0

Table 5. Hyperfine parameters calculated from the Mössbauer spectrum of wollastonite NYAD G. Isomer shift (δ), quadrupole splitting (Δ), half linewidth at half maximum (Γ_+) and, the relative area (A). δ is quoted to metallic α-Fe.

Doublet	δ (mm/s)	Δ (mm/s)	Γ_+ (mm/s)	A (%)	Attributions
Db1	0.41 ± 0.01	0.56 ± 0.03	0.12 ± 0.01	31 ± 2	Fe^{3+} octahedral (*M*1,*M*2,*M*3)
Db2	1.09 ± 0.04	2.26 ± 0.09	0.31 ± 0.08	46 ± 2	Fe^{2+} octahedral (*M*3)
Db3	1.26 ± 0.01	2.76 ± 0.04	0.11 ± 0.02	23 ± 2	Fe^{2+} octahedral (*M*1)

Among the considered mineral species, the difference in the dissolution time of wollastonite NYAD G with respect to amphibole asbestos is remarkable. After 383 d (for a 3.17 µm thick fibre) or 30 d (for a 0.25 µm thick fibre), the wollastonite fibres are completely dissolved. On the other hand, asbestos amphiboles totally dissolve only after 50 y (Table 3). Conversely, the dissolution rate and estimated lifetime of wollastonite NYAD G are similar to those estimated for chrysotile [71].

The total content of elemental iron in the wollastonite NYAD G is 0.38 wt% (Fe^{2+} = 0.26 wt%; Fe^{3+} = 0.12 wt%). While the total content of elemental silicon is 23.73 wt%. Considering that the total dissolution time of wollastonite fibres is 1.05 y (383 d), the

estimated velocity of release of Fe and Si from the dissolving wollastonite fibres inside the cytoplasmic space is 0.36 and 22.60, respectively.

3.2. Toxicity/Pathogenicity Potential of Wollastonite NYAD G

Table 1 reports the FPTI index calculated for the wollastonite NYAD G and the normalized score FPTIi associated to each parameter of the FPTI model [24]. The same data concerning two mineral fibres (i.e., chrysotile from Balangero, Italy, and asbestos tremolite from Val D'Ala, Italy) currently recognised by the IARC as carcinogenic to humans, have been reported for comparison (Table 1). The sum of the values yields an FPTI associated with the mineral fibre. The classification of mineral fibres in increasing order of toxicity potential is: wollastonite NYAD G (FPTI = 2.12) < Balangero chrysotile (2.35) < Val D'Ala tremolite (FPTI = 2.88). According to applied model [24], FPTI $\leq$ 2.00 concerns mineral fibres that are assumed to have no toxic/pathogenic effects. Given the error (0.18) associated with the calculation of the FPTI, wollastonite NYAD G can also be considered a 'safe' mineral fibre [24].

The main differences between the positive reference mineral fibres (i.e., Balangero chrysotile and Val D'Ala tremolite) and wollastonite NYAD G concern the average width of the fibres, content of reactive metals and dissolution rate (Table 1).

Balangero chrysotile and Val D'Ala tremolite display an asbestiform habit (i.e., these minerals grow in a fibrous bundle of flexible, long, thin crystals) which makes them easily inhalable. These particles thanks to their small width (W < 1 μm), reach the deep respiratory system, settle there and cause cell damage [24,72]. In contrast, wollastonite fibres are too wide (average W = 3.74 μm) to pass through the upper airways [24,72]. The deposition of a mineral fibre is related to is equivalent aerodynamic diameter (D_{ae}) [72]. Applying the equation of Gonda and Abd El Khalik [89] to a wollastonite NYAD G fibre with W = 3.74 μm and ρ = 2.98 g/cm^3, the D_{ae} obtained is 11.4 μm [72]. Since particles with D_{ae} > 5 tend to settle in the nasal respiratory tract, wollastonite fibres are expected to be filtered by the nasal epithelial barrier [72].

Chemical reactivity of mineral fibres (and associated adverse effects *in vivo*/*in vitro*) is related to the catalytic activity of Fe^{2+} for the production of ROS [24]. Both Balangero chrysotile and Val d'Ala tremolite have significant amounts of structural Fe^{2+} and, therefore, are expected to have high chemical reactivity [90]. Namely, the FeO wt% of wollastonite NYAD G is 0.33 wt%, whereas it is 2.5 wt% for Balangero chrysotile and 2.0 wt% for Val D'Ala tremolite.

Recent studies have shown that octahedral sites of asbestos fibres may host potentially toxic metals that can be released during fibre dissolution [29]. These toxic metals contribute, together with iron, to the potential toxicity of Balangero chrysotile and Val d'Ala tremolite [24,29]. On the contrary, the low metal content found in wollastonite NYAD G makes its fibres of low reactivity [24,29].

The dissolution rate of wollastonite NYAD G is similar to that of chrysotile while the difference with amphibole asbestos is remarkable (Table 3; lifetime calculated for a 0.25 μm thick fibre). Estimated lifetime of wollastonite NYAD G and Balangero chrysotile is 30 d and 124 d, respectively. On the other hand, Val d'Ala tremolite totally dissolve after 49 y (Table 3). This implies that wollastonite fibres are not biopersistent in lung environment, and therefore less potent in inducing chronic inflammation. As noted above, chrysotile also has a low biodurability (Table 3), however, it has a higher FPTI index than fibrous wollastonite (Table 1). To a first approximation, the lack of biopersistence should also make chrysotile a safe mineral fibre. However, during phagocytosis, the chrysotile behaves like a carrier that releases its metal cargo into the lung environment (e.g., Fe, Co, Cu, Cr and Ni), mimicking the toxicity behaviour of nanoparticles [29]. These metals, when released into the cytoplasmic space, catalyse the production of ROS/RNS, inducing an acute toxic effect involving cellular injury and DNA damage [24,29].

3.3. DNA Damage Quantification

Studies on asbestos have shown that mineral fibres can induce DNA damage [12]. There are many forms of DNA damage, but DNA double strand breaks (DSB) are one of the most damaging lesions because they affect both strands of the DNA helix [73]. This type of DNA damage can lead to cell death through apoptosis, but if the cell survives and the injury is not repaired (or is repaired incorrectly), DNA information can be compromised leading to mutations and eventually cancer [73]. To date, only preliminary data on the potential genotoxicity of fibrous wollastonite are available [16,46,53]. In the present work, in order to assess the potential genotoxicity of wollastonite NYAD G, a γH2AX assay [73] was performed on THP-1 cells exposed to wollastonite fibres for 24 h. Thus, after the treatment of THP-1 macrophages in the presence or absence of 50 µg/mL of mineral fibres, the DNA double strand breaks (DSB) in M0-THP-1 macrophages (Figure 5) were quantitatively evaluated by confocal microscopy through the staining of the γ-H2AX foci. The foci rate of treated and untreated cells was then quantified and as expected, the macrophages challenged with crocidolite UICC showed a significant high rate of DSB, while no significant differences with respect to control cells were observed in wollastonite NYAD G treatment. In detail, the fold increase of foci rate measured in treated macrophages with respect to control cells was ~8.9 for crocidolite UICC (white bar, $p < 0.0001$ vs. C) and ~0.7 for wollastonite NYAD G (dotted bar, $p < 0.28$ vs. C). These data clearly indicate that crocidolite UICC is able to significantly increase DNA damage in THP-1 cells after 24 h, whereas wollastonite NYAD G shows no acute DNA damage at the same incubation time and under the same experimental conditions.

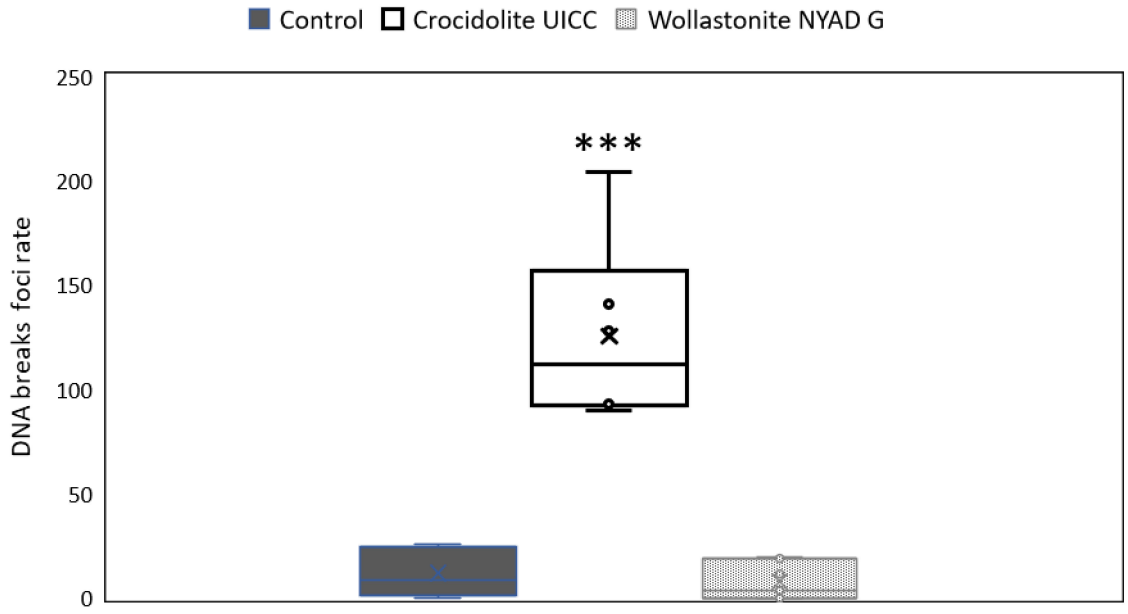

Figure 5. Quantification of DNA double-strand breaks by confocal microscopy analysis of THP-1 cells. Results are expressed as the rate of double-strand breaks in the DNA counted in the nuclei of untreated cells (control, grey bar) or cells treated with 50 µg/mL of crocidolite UICC fibers (white bar) or of wollastonite NYAD G fibers (dotted bar) for 24 h. Bars represent the mean ± S.D. of the total number of foci (stained in green by an anti-γH2AX antibody, not shown) in the nuclei of cells acquired in six different microphotographs obtained using a Leica TCS SL confocal microscope. Asterisks indicate significance in Tukey test (ANOVA $p < 0.000001$; Tukey vs. C, *** $p < 0.0001$).

4. Discussion

To date, the most commonly used experimental treatments (i.e., samples that are the subject of the experiment) for *in vitro* studies on mineral fibres are as follows: cells treated with the tested fibre, "untreated" control (i.e., cells + media + reagent) and positive control (which usually involves the UICC crocidolite standard). Similar experimental

treatments are also commonly adopted for *in vivo* tests. However, as emphasised by many official methods and best practices concerning *in vitro*/*in vivo* systems, experimental design requires the use of a negative control [41,42]. In this context, the aim of the present work is to propose a suitable reference material that can be used as a negative control for biological and biomedical studies involving mineral fibres. After careful evaluation of the various naturally occurring non-hazardous mineral fibres, fibrous wollastonite was found to be suitable for this purpose. An ideal negative control for bioassays has the following characteristics: it is non-toxic, does not contain toxic impurities, is easy to find in large quantities and its composition is well known [41]. All of these properties are possessed by wollastonite NYAD G. Indeed, this mineral fibre is easy to find as it is marketed by NYCO as a raw material for various industrial applications. As shown by the results of the TG and XRPD analyses, wollastonite NYAD G is virtually pure as it consists of wollastonite-1A with only about 1wt% calcite (a non-toxic substance). Data obtained from EMPA show that wollastonite NYAD G does not contain significant concentrations of potentially toxic elements that can be released into lung tissue following inhalation of its fibres.

The assessment of the toxicity/pathogenicity potential of wollastonite NYAD G was performed using the FPTI model (Table 1). A quick comparison with previously evaluated mineral fibres shows that wollastonite NYAD G is less hazardous than asbestos minerals. As shown by Gualtieri [24], all the amphibole asbestos has FPTI values >2.50, while chrysotile asbestos samples have values in the range 2.20–2.45. The FPTI of wollastonite NYAD G (i.e., 2.12) is lower than that of all other fibres and in line with the designated threshold value for non-toxic and non-pathogenic fibres (FPTI = 2.00). Therefore, according to the results of the applied FPTI model, wollastonite NYAD G can be considered a mineral fibre with low toxicity/pathogenicity potential [24]. As a matter of fact, the result obtained from the FPTI model converges with the IARC assessments, but it should be emphasised that to date there is no conclusive evidence that fibrous wollastonite has no toxicity and pathogenicity effect *in vivo* [16,46].

The FPTI of wollastonite was previously calculated by Gualtieri [24] using literature data to estimate FPTI parameter scores (Table 1). The FPTI obtained was 1.92 (0.30). Since this index is slightly different from that obtained in the present work (i.e., 2.12), it is appropriate to compare the analytical data obtained in this work with those found in the literature for wollastonite NYAD G. For this purpose, a suitable reference is the work of Maxim et al. [46], which provides the morphology, chemical compositions and SSA of several commercial wollastonite samples, including wollastonite NYAD G. In addition, a precious document is the technical data sheet (TDS) of wollastonite NYAD G provided by NYCO Minerals Inc. [87]. TDS provides several technical properties (e.g., density, water solubility, hardness, meting point, etc.) and chemical composition of wollastonite NYAD G. Although Maxim et al. [46] and the TDS are useful references, it must be underlined that these documents do not provide any information about the analytical methods used for the characterisation of wollastonite NYAD G. This omission makes it difficult to discern whether the discrepancies between the compared values are due to analytical error or a different method of data acquisition.

As widely recognised in the literature, wollastonite is characterised by acicular or fibrous particles [43,46,87]. This description is in line with that obtained by us through SEM analysis. The wollastonite NYAD G fibres observed by SEM have the following average size: L = 46.6 μm, W = 3.74 μm and aspect ratio 13:1. In contrast, reference [46] shows that wollastonite NYAD G has L = 60 μm, W = 6.2 μm and aspect ratio 15:1. Despite this discrepancy, both morphometric evaluations show that the sample has a size that exceeds the morphometric threshold values set by the FPTI model, i.e., L = 20 μm and D = 3 μm [24]. This implies that the wollastonite NYAD G fibres are long enough to induce a chronic alveolar or pleural inflammatory effect, but are too thick to reach and penetrate the alveolar and pleural sacs [24,72].

ρ and SSA of the wollastonite NYAD G provided by the TDS are 2.90 g/cm^3 and 0.4 m^2/g, respectively [87]. These values agree well with that obtained in our investigations, i.e., ρ = 2.98 g/cm^3 and SSA = 0.5 m^2/g.

Like other mineral fibres [91], wollastonite NYAD G in contact with the ALF solution at pH 4.5 and 7 results in negative values of zeta potential, i.e., −8.96 and −18.7 mV, respectively. Negative zeta potential values were also found when water was used as a dispersant (Figure 4). According to Buthelezi [77], the zeta potential of wollastonite in water varies from −20 to −35 mV and decreases with increasing pH (i.e., from 3 to 9). When placed in an organic solution (i.e., dodecylamine), wollastonite shows slightly less negative zeta potentials than those observed in water, and the values range from about –5 to −20 mV [77]. A similar behaviour of the zeta potential was observed in our study for the wollastonite NYAD G, i.e., in the pH range of 3–9, the zeta potential in water varies from −24 to −36 mV, while −0.4 to −25 mV in ALF solution.

Table 4 compares the chemical composition of wollastonite obtained from EMPA and those reported in TDS. Small but significant differences exist between the two chemical compositions, mainly for elements such as Al, K and Ti. The data provided by TDS probably refer to the bulk analysis of the sample (probably obtained from X-ray fluorescence analysis, as suggested by the presence of the LOI value), so the values of Al, K and Ti are slightly higher than expected because they are influenced by the impurities present in the sample analysed (e.g., garnet). In contrast, in the chemical analyses obtained by EMPA, Al, K and Ti are not measured because only wollastonite fibres were analysed.

The fast dissolution of wollastonite in ALF solution observed in our *in vitro* acellular study is in line with that observed in the literature [92]. Wollastonite is the ideal mineral phase for mineral–solution interaction studies, because it has a simple composition and structure and reacts very quickly [92]. Consequently, comprehensive descriptions of the behaviour of wollastonite fibres in acidic solutions can be found in the extensive literature concerning the mechanisms and kinetics of mineral dissolution [92–96]. It is generally recognised that the dissolution rate of wollastonite is a function of the environmental pH and is higher under acidic conditions [92–96]. Several experimental studies show that the dissolution of wollastonite in acidic solution is controlled by the leaching of Ca^{2+} through metal-proton exchange [53,92]. This exchange reaction leads to the formation of a silica-rich layer that grows indefinitely, preventing the dissolution of wollastonite from reaching a steady state and leading to the total extraction of Ca^{2+} from the structure [92]. Since wollastonite is highly soluble in acidic conditions, its dissolution is expected during phagocytosis processes, where the environment is approximately pH 4.5.

Although our biodurability tests on wollastonite (based on *in vitro* acellular experiment) are not fully comparable with those found in the literature (which are based on in vivo studies [46,97]), the general consensus is that the biodurability of wollastonite is significantly lower than that of positive carcinogens such as amphibole asbestos. Studies on Wistar rats, showed that the rate of clearance of wollastonite NYAD G was 14 times higher than that of crocidolite [97]. A higher rate of clearance of wollastonite with respect to amphibole asbestos was confirmed by biopersistence studies using CS57B1/6 mice [98].

Results of the *in vitro* genotoxicity test (Figure 5) point out a safer biological behaviour of wollastonite NYAD G, once again suggesting its possible use as a negative control in toxicological experiments *in vitro* and in vivo.

Overall, the results of the characterisation of wollastonite NYAD G performed in this study are in good agreement with the literature data. The toxicity/pathogenicity potential of fibrous wollastonite as assessed by in the present work is consistent with the assessment of the IARC [16] and the various toxicity studies performed to date [46].

5. Conclusions

To date, most toxicity and carcinogenicity studies involving mineral fibres are designed without a negative control. The aim of this study was to assess if wollastonite NYAD G can be a suitable material to be used as a negative control. For this purpose, a complete

characterisation of the commercially available wollastonite NYAD G has been accomplished. The results agree with data found in the literature and confirm that the sample consists of wide elongated particles, with low specific surface area, low metal content and low biodurability. The behaviour of the zeta potential in water and ALF is similar to that observed for other mineral fibres and shows negative values throughout the pH range considered. XRPD and TG-DTA analysis showed that the sample consists of wollastonite-1A in association with calcite.

The selection of the negative control should primarily consider the toxicity/pathogenicity potential of the selected material. This assessment was achieved through the application of the FPTI model. The FPTI was calculated on the basis of the acquired analytical data, which showed that wollastonite NYAD G does not possess the chemical-physical characteristics of toxic fibres known to cause adverse effects in vivo. The estimated FPTI is below the values found for hazardous mineral fibres and confirms that wollastonite NYAD G has negligible toxicity/pathogenicity potential. In particular, the potential of wollastonite NYAD G fibres in inducing MM is extremely low as their width (W > 3 μm) does not allow them to reach and penetrate the pleural space. The inert behaviour of wollastonite NYAD G was confirmed by the γ-H2AX foci assay. Compared to crocidolite, wollastonite NYAD G has a very low genotoxic potential.

Supplementary Materials: The following are available online at https://www.mdpi.com/article/10.3390/min11121378/s1, Figure S1: As reported in Gualtieri [99] presentative SEM image and EDX spectrum of a calcite crystal found in the sample, Figure S2: Mössbauer spectrum of wollastonite NYAD G, Figure S3: XPS spectrum of wollastonite NYAD G, Figure S4: UV-Vis spectrum of wollastonite NYAD G, Figure S5: Dissolution curve of wollastonite NYAD G, Table S1: EMPA spot analyses.

Author Contributions: Conceptualization, D.D.G. and A.F.G.; methodology, A.F.G. and D.D.G.; validation, A.F.G.; formal analysis, V.S., D.M., U.T., M.H., L.N., L.P., S.S., S.M., M.L.G. and D.D.G.; data curation, D.D.G.; writing—original draft preparation, D.D.G.; writing—review and editing, D.D.G. and A.F.G.; supervision, A.F.G. and D.D.G.; project administration, A.F.G.; funding acquisition, A.F.G. All authors have read and agreed to the published version of the manuscript.

Funding: This research was conducted under the project "Fibres a Multidisciplinary Mineralogical, Crystal-Chemical and Biological Project to Amend the Paradigm of Toxicity and Cancerogenicity of Mineral Fibres" (PRIN: PROGETTI DI RICERCA DI RILEVANTE INTERESSE NAZIONALE—Bando 2017—Prot. 20173X8WA4).

Acknowledgments: We warmly acknowledge the two reviewers for their advices to improve the manuscript. Rispendente A., Paganelli E. and Giovanardi T. are kindly acknowledged for their support in carrying out the EMPA analyses.

Conflicts of Interest: The authors declare no conflict of interest.

References

1. Baumann, F.; Ambrosi, J.P.; Carbone, M. Asbestos is not just asbestos: An unrecognised health hazard. *Lancet Oncol.* **2013**, *14*, 576–578. [CrossRef]
2. Gunter, M.E. Elongate mineral particles in the natural environment. *Toxicol. Appl. Pharmacol.* **2018**, *361*, 157–164. [CrossRef] [PubMed]
3. Di Giuseppe, D.; Harper, M.; Bailey, M.; Erskine, B.; Della Ventura, G.; Ardit, M.; Pasquali, L.; Tomaino, G.; Ray, R.; Mason, H.; et al. Characterization and assessment of the potential toxicity/pathogenicity of fibrous glaucophane. *Environ. Res.* **2019**, *178*, 108723. [CrossRef]
4. Mattioli, M.; Giordani, M.; Dogan, M.; Cangiotti, M.; Avella, G.; Giorgi, R.; Dogan, A.U.; Ottaviani, M.F. Morpho-chemical characterization and surface properties of carcinogenic zeolite fibers. *J. Hazard. Mater.* **2016**, *306*, 140–148. [CrossRef]
5. Pacella, A.; Ballirano, P. Chemical and structural characterization of fibrous richterite with high environmental and health relevance from Libby, Montana (USA). *Period. Mineral.* **2016**, *85*, 169–177.
6. Cametti, G.; Pacella, A.; Mura, F.; Rossi, M.; Ballirano, P. New morphological, chemical, and structural data of woolly erionite-Na from Durkee, Oregon, USA. *Am. Mineral.* **2013**, *98*, 2155–2163. [CrossRef]
7. Petriglieri, J.R.; Laporte-Magoni, C.; Salvioli-Mariani, E.; Ferrando, S.; Tomatis, M.; Fubini, B.; Turci, F. Morphological and chemical properties of fibrous antigorite from lateritic deposit of New Caledonia in view of hazard assessment. *Sci. Total Environ.* **2021**, *777*, 146185. [CrossRef]

8. Comba, P.; Gianfagna, A.; Paoletti, L. Pleural mesothelioma cases in Biancavilla are related to a new fluoro-edenite fibrous amphibole. *Arch. Environ. Health* **2003**, *58*, 229–232. [CrossRef] [PubMed]
9. Larson, T.C.; Antao, V.C.; Bove, F.J. Vermiculite worker mortality: Estimated effects of occupational exposure to Libby amphibole. *J. Occup. Environ. Med.* **2010**, *52*, 555–560. [CrossRef] [PubMed]
10. Suzuki, Y. Carcinogenic and fibrogenic effects of zeolites: Preliminary observations. *Environ. Res.* **1982**, *27*, 433–445. [CrossRef]
11. International Agency for Research on Cancer. Asbestos (chrysotile, amosite, crocidolite, tremolite, actinolite, and anthophyllite). In *IARC Monographs*; International Agency for Research on Cancer: Lyon Cedex, France, 2012; Volume 100, pp. 219–309.
12. International Agency for Research on Cancer. Erionite. In *IARC Monographs*; International Agency for Research on Cancer: Lyon Cedex, France, 2012; Volume 100, pp. 311–315.
13. International Agency for Research on Cancer. Fluoro-edenite. In *IARC Monographs*; International Agency for Research on Cancer: Lyon Cedex, France, 2017; Volume 111, pp. 215–242.
14. Carbone, M.; Emri, S.; Dogan, A.U.; Steele, I.; Tuncer, M.; Pass, H.I.; Baris, Y.I. A mesothelioma epidemic in Cappadocia: Scientific developments and unexpected social outcomes. *Nat. Rev. Cancer* **2007**, *7*, 147–154. [CrossRef] [PubMed]
15. International Agency for Research on Cancer. Sepiolite. In *IARC Monographs*; International Agency for Research on Cancer: Lyon Cedex, France, 1997; Volume 68, pp. 267–282.
16. International Agency for Research on Cancer. Wollastonite. In *IARC Monographs*; International Agency for Research on Cancer: Lyon Cedex, France, 1997; Volume 68, pp. 283–306.
17. International Agency for Research on Cancer. Zeolite other than erionite. In *IARC Monographs*; International Agency for Research on Cancer: Lyon Cedex, France, 1997; Volume 68, pp. 307–336.
18. International Agency for Research on Cancer. Palygorskite (Attapu1gite). In *IARC Monographs*; International Agency for Research on Cancer: Lyon Cedex, France, 1997; Volume 68, pp. 245–266.
19. International Agency for Research on Cancer. Preamble. In *IARC Monographs*; International Agency for Research on Cancer: Lyon Cedex, France, 2012; Volume 100, pp. 11–34.
20. Carbone, M.; Adusumilli, P.S.; Alexander, H.R., Jr.; Baas, P.; Bardelli, F.; Bononi, A.; Bueno, R.; Felley-Bosco, E.; Galateau-Salle, F.; Jablons, D.; et al. Mesothelioma: Scientific clues for prevention, diagnosis, and therapy. *CA Cancer J. Clin.* **2019**, *69*, 402–429. [CrossRef] [PubMed]
21. Carbone, M.; Yang, H. Biological activities of asbestos and other mineral fibres. In *Mineral Fibres: Crystal Chemistry, Chemical-Physical Properties, Biological Interaction and Toxicity*; Gualtieri, A.F., Ed.; European Mineralogical Union: London, UK, 2017; pp. 435–445.
22. Jablonski, R.P.; Kim, S.J.; Cheresh, P.; Kamp, D.W. Insights into mineral fibre-induced lung epithelial cell toxicity and pulmonary fibrosis. In *Mineral Fibres: Crystal Chemistry, Chemical-Physical Properties, Biological Interaction and Toxicity*; Gualtieri, A.F., Ed.; European Mineralogical Union: London, UK, 2017; pp. 447–500.
23. Xue, J.; Patergnani, S.; Giorgi, C.; Suarez, J.; Goto, K.; Bononi, A.; Tanji, M.; Novelli, F.; Pastorino, S.; Xu, R.; et al. Asbestos induces mesothelial cell transformation via HMGB1-driven autophagy. *Proc. Natl. Acad. Sci. USA* **2020**, *117*, 25543–25552. [CrossRef]
24. Gualtieri, A.F. Towards a quantitative model to predict the toxicity/pathogenicity potential of mineral fibers. *Toxicol. Appl. Pharmacol.* **2018**, *361*, 89–98. [CrossRef] [PubMed]
25. Stanton, M.F.; Layard, M.; Tegeris, A.; Miller, E.; May, M.; Morgan, E.; Smith, A. Relation of particle dimension to carcinogenicity in amphibole asbestoses and other fibrous minerals. *J. Natl. Cancer Inst.* **1981**, *67*, 965–975.
26. Krombach, F.; Münzing, S.; Allmeling, A.M.; Gerlach, J.T.; Behr, J.; Dörger, M. Cell size of alveolar macrophages: An interspecies comparison. *Environ. Health Persp.* **1997**, *105*, 1261–1263.
27. Donaldson, K.; Murphy, F.A.; Duffin, R.; Poland, C.A. Asbestos, carbon nanotubes and the pleural mesothelium: A review of the hypothesis regarding the role of long fibre retention in the parietal pleura, inflammation and mesothelioma. *Part. Fibre Tox.* **2010**, *7*, 5. [CrossRef] [PubMed]
28. Shukla, A.; Gulumian, M.; Hei, T.K.; Kamp, D.; Rahman, Q.; Mossman, B.T. Multiple roles of oxidants in the pathogenesis of asbestos-induced diseases. *Free Radic. Bio. Med.* **2003**, *34*, 1117–1129. [CrossRef]
29. Gualtieri, A.F.; Lusvardi, G.; Zoboli, A.; Di Giuseppe, D.; Lassinantti Gualtieri, M. Biodurability and release of metals during the dissolution of chrysotile, crocidolite and fibrous erionite. *Environ. Res.* **2019**, *171*, 550–557. [CrossRef] [PubMed]
30. Turci, F.; Tomatis, M.; Lesci, I.S.; Roveri, N.; Bice, F. The iron-related molecular toxicity mechanism of synthetic asbestos nanofibres: A model study for high-aspect-ratio nanoparticles. *Chem. Eur. J.* **2011**, *17*, 250–358. [CrossRef]
31. Mossman, B.T.; Pugnaloni, A. In vitro biological activity and mechanisms of lung and pleural cancers induced by mineral fibres. In *Mineral Fibres: Crystal Chemistry, Chemical-Physical Properties, Biological Interaction and Toxicity*; Gualtieri, A.F., Ed.; European Mineralogical Union: London, UK, 2017; pp. 261–306.
32. Capella, S.; Belluso, E.; Bursi Gandolfi, N.; Tibaldi, E.; Mandrioli, D.; Belpoggi, F. In vivo biological activity of mineral fibres. In *Mineral Fibres: Crystal Chemistry, Chemical-Physical Properties, Biological Interaction and Toxicity*; Gualtieri, A.F., Ed.; European Mineralogical Union: London, UK, 2017; pp. 307–346.
33. Cardinali, G.; Kovacs, D.; Maresca, V.; Flori, E.; Dell'Anna, M.L.; Campopiano, A.; Casciardi, S.; Spagnoli, G.; Torrisi, M.L.; Picardo, M. Differential in vitro cellular response induced by exposure to synthetic vitreous fibers (SVFs) and asbestos crocidolite fibers. *Exp. Mol. Pathol.* **2006**, *81*, 31–41. [CrossRef] [PubMed]

34. Gualtieri, A.F.; Zoboli, A.; Filaferro, M.; Benassi, M.; Scarfi, S.; Mirata, S.; Avallone, R.; Vitale, G.; Bailey, M.; Harper, M.; et al. In vitro toxicity of fibrous glaucophane. *Toxicology* **2021**, *454*, 152743. [CrossRef] [PubMed]
35. Cardile, V.; Renis, M.; Scifo, C.; Lombardo, L.; Gulino, R.; Mancari, B.; Panico, A. Behaviour of the new asbestos amphibole fluoro-edenite in different lung cell systems. *Int. J. Biochem. Cell Biol.* **2004**, *36*, 849–860. [CrossRef] [PubMed]
36. Bernstein, D.M.; Pavlisko, E.N. Differential pathological response and pleural transport of mineral fibres. In *Mineral Fibres: Crystal Chemistry, Chemical-Physical Properties, Biological Interaction and Toxicity*; Gualtieri, A.F., Ed.; European Mineralogical Union: London, UK, 2017; pp. 2417–2434.
37. Bernstein, D.M.; Toth, B.; Rogers, R.A.; Kling, D.E.; Kunzendorf, P.; Phillips, J.I.; Ernst, H. Evaluation of the exposure, dose-response and fate in the lung and pleura of chrysotile-containing brake dust compared to TiO_2, chrysotile, crocidolite or amosite asbestos in a 90-day quantitative inhalation toxicology study—Interim results Part 1: Experimental design, aerosol exposure, lung burdens and BAL. *Toxicol. Appl. Pharmacol.* **2020**, *387*, 11487.
38. Gavett, S.H.; Parkinson, C.U.; Willson, G.A.; Wood, C.E.; Jarabek, A.M.; Roberts, K.C.; Kodavani, U.P.; Dodd, D.E. Persistent effects of Libby amphibole and amosite asbestos following subchronic inhalation in rats. *Part. Fibre Toxicol.* **2015**, *13*, 1–20. [CrossRef] [PubMed]
39. Thompson, J.K.; MacPherson, M.B.; Beuschel, S.L.; Shukla, A. Asbestos-induced mesothelial to fibroblastic transition is modulated by the inflammasome. *Am. J. Pathol.* **2017**, *187*, 665–678. [CrossRef] [PubMed]
40. Napolitano, A.; Pellegrini, L.; Dey, A.; Larson, D.; Tanji, M.; Flores, E.G.; Kendrick, B.; Lapid, D.; Powers, A.; Kanodia, S.; et al. Minimal asbestos exposure in germline BAP1 heterozygous mice is associated with deregulated inflammatory response and increased risk of mesothelioma. *Oncogene* **2016**, *35*, 1996–2002. [CrossRef]
41. Eskes, C.; Boström, A.C.; Bowe, G.; Coecke, S.; Hartung, T.; Hendriks, G.; Pamies, D.; Piton, A.; Rovida, C. Good cell culture practices & *in vitro* toxicology. *Toxicol. Vitr.* **2017**, *45*, 272–277.
42. Lipsitch, M.; Tchetgen, E.T.; Cohen, T. Negative controls: A tool for detecting confounding and bias in observational studies. *Epidemiology* **2010**, *21*, 383–388. [CrossRef]
43. Deer, W.A.; Howie, R.A.; Zussman, J. *An Introduction to the Rock-Forming Minerals*, 3rd ed.; Mineralogical Society of Great Britain and Ireland: London, UK, 2013; pp. 132–135.
44. Angel, R.J. Structural variation in wollastonite and bustamite. *Min. Mag.* **1985**, *49*, 37–48. [CrossRef]
45. Mazzucato, E.; Gualtieri, A.F. Wollastonite polytypes in the CaO-SiO_2 system. *Phys. Chem. Miner.* **2000**, *27*, 565–574. [CrossRef]
46. Maxim, L.D.; Niebo, R.; Utell, M.J.; McConnell, E.E.; LaRosa, S.; Segrave, A.M. Wollastonite toxicity: An update. *Inhal. Toxicol.* **2014**, *26*, 95–112. [CrossRef] [PubMed]
47. Somtürk, S.M.; Emek, I.Y.; Senler, S.; Eren, M.; Kurt, S.Z.; Orbay, M. Effect of wollastonite extender on the properties of exterior acrylic paints. *Prog. Org. Coat.* **2016**, *93*, 34–40. [CrossRef]
48. Xue, W.; Liu, X.; Zheng, X.; Ding, C. In vivo evaluation of plasma-sprayed wollastonite coating. *Biomaterials* **2005**, *26*, 3455–3460. [CrossRef]
49. Miu, D.M.; Jinga, S.I.; Voicu, G.; Iordache, F. Characteristics of wollastonite ceramic coatings obtained by pulsed laser deposition. *J. Inorg. Organomet. Polym. Mater.* **2021**, *31*, 1601–1607. [CrossRef]
50. Taghiyari, H.R.; Kalantari, A.; Ershad-Langroudi, A. Effects of wollastonite nanofibers on biological resistance of historical paper against Aspergillus niger. *Lignocellulose* **2014**, *3*, 111–118.
51. Taghiyari, H.R.; Majidi, R.; Esmailpour, A.; Samadi, Y.S.; Jahangiri, A.; Papadopoulos, A.N. Engineering composites made from wood and chicken feather bonded with UF resin fortified with wollastonite: A novel approach. *Polymers* **2020**, *12*, 857. [CrossRef] [PubMed]
52. Dasari, A.; Misra, D.K.; Rohrmann, J. Scratch deformation characteristics of micrometric wollastonite-reinforced ethylene-propylene copolymer compositess. *Polym. Eng. Sci.* **2004**, *9*, 1738–1748. [CrossRef]
53. Maxim, L.D.; McConnell, E.E. A review of the toxicology and epidemiology of wollastonite. *Inhal. Toxicol.* **2005**, *17*, 451–466. [CrossRef]
54. Amin, A.M.; El-Amir, A.A.; Karunakaran, G.; Kuznetsov, D.; Ewais, E.M. In-vitro evaluation of wollastonite nanopowder produced by a facile process using cheap precursors for biomedical applications. *Ceram. Int.* **2021**, *47*, 18684–18692. [CrossRef]
55. Nikhil, P.S.; Ravichandran, P.T.; Krishnan, K.D. Stabilisation and characterisation of soil using wollastonite powder. *Mater. Today Proc.* **2021**, *40*, S161–S166. [CrossRef]
56. Hayder, A.; Vanderburgt, S.; Santos, R.M.; Chiang, Y.W. Phosphorous runoff risk assessment and its potential management using wollastonite according to geochemical modeling. *Open Agric.* **2019**, *4*, 787–794. [CrossRef]
57. Haque, F.; Santos, R.M.; Chiang, Y.W. CO_2 sequestration by wollastonite-amended agricultural soils—An Ontario field study. *Int. J. Greenh. Gas Control* **2020**, *97*, 103017. [CrossRef]
58. USGS National Minerals Information Center. Available online: https://pubs.usgs.gov/periodicals/mcs2020/mcs2020-wollastonite.pdf (accessed on 26 July 2021).
59. Vitra, B.R.; Wollastonite. U.S. *Geological Survey Minerals Yearbook*; 2000; pp. 84.1–84.2. Available online: https://s3-us-west-2.amazonaws.com/prd-wret/assets/palladium/production/mineral-pubs/wollastonite/860400.pdf (accessed on 26 July 2021).

60. Whitney, P.R.; Olmsted, J.F. Wollastonite Deposits of the Northeastern Adirondacks. In *Field Trip Guidebook for 67th Annual Meeting of the New York State Geological Association*; Union College: Schenectady, NY, USA, 1995; pp. 25–38. Available online: https://ottohmuller.com/nysga2ge/Files/1995/NYSGA%201995%20A2%20-%20Wollastonite%20Deposits%20of%20the%20Northeastern%20Adirondacks.pdf (accessed on 26 July 2021).
61. Peck, W.H.; Bailey, E. Origin of the Lewis wollastonite deposit. In *Field Trip Guidebook for the 80th Annual Meeting of the New York State Geological Association: September 26–28, 2008*; New York State Geological Association: New York, NY, USA, 2008; pp. 130–135. Available online: https://ottohmuller.com/nysga2ge/Files/2008/NYSGA%202008%2011.%20%20Origin%20of%20the%20Lewis%20Wollastonite%20Deposit.pdf (accessed on 26 July 2021).
62. Degen, T.; Sadki, M.; Bron, E.; König, U.; Nénert, G. The HighScore Suite. *Powder Diffr.* **2014**, *29*, 13–18. [CrossRef]
63. National Institute of Mental Health. ImageJ. Available online: https://imagej.nih.gov/ij/ (accessed on 14 July 2021).
64. Brunauer, S.; Emmet, P.H.; Teller, E. Adsorption of gases in multimolecular layers. *J. Am. Chem. Soc.* **1938**, *60*, 309–319. [CrossRef]
65. Di Giuseppe, D.; Zoboli, A.; Nodari, L.; Pasquali, L.; Sala, O.; Ballirano, P.; Malferrari, D.; Raneri, S.; Hanuskova, M.; Gualtieri, A.F. Characterization and assessment of the potential toxicity/pathogenicity of Russian commercial chrysotile. *Am. Min.* **2021**, *106*, 1606–1621. [CrossRef]
66. Marques, M.R.; Loebenberg, R.; Almukainzi, M. Simulated biological fluids with possible application in dissolution testing. *Dissolut. Technol.* **2011**, *18*, 15–28. [CrossRef]
67. Rancourt, D.; McDonald, A.M.; Lalonde, A.E.; Ping, J.Y. Mössbauer absorber thicknesses for accurate site populations in Fe-bearing minerals. *Am. Min.* **1993**, *78*, 1–7.
68. Lagarec, K.; Rancourt, D.G. *Recoil—Mössbauer Spectral Analysis Software for Windows*; Department of Physics, University of Ottawa: Ottawa, ON, USA, 1998.
69. Pirngruber, G.D.; Roy, P.K.; Prins, R. On determining the nuclearity of iron sites in Fe-ZSM-5—A critical evaluation. *Phys. Chem. Chem. Phys.* **2006**, *8*, 3939–3950. [CrossRef]
70. Borghi, E.; Occhiuzzi, M.; Foresti, E.; Lesci, I.G.; Roveri, N. Spectroscopic characterization of Fe-doped synthetic chrysotile by EPR, DRS and magnetic susceptibility measurements. *Phys. Chem. Chem. Phys.* **2010**, *12*, 227–238. [CrossRef]
71. Gualtieri, A.F.; Pollastri, S.; Bursi Gandolfi, N.; Lassinantti Gualtieri, M. In vitro acellular dissolution of mineral fibres: A comparative study. *Sci. Rep.* **2018**, *8*, 7071. [CrossRef]
72. Gualtieri, A.F.; Mossman, B.T.; Roggli, V.L. Towards a general model for predicting the toxicity and pathogenicity of minerals fibres. In *Mineral Fibres: Crystal Chemistry, Chemical-Physical Properties, Biological Interaction and Toxicity*; Gualtieri, A.F., Ed.; European Mineralogical Union: London, UK, 2017; pp. 501–526.
73. Garcia-Canton, C.; Anadón, A.; Meredith, C. γH2AX as a novel endpoint to detect DNA damage: Applications for the assessment of the in vitro genotoxicity of cigarette smoke. *Toxicol. Vitr.* **2012**, *26*, 1075–1086. [CrossRef]
74. Földvári, M. *Handbook of Thermogravimetric System of Minerals and Its Use in Geological Practice*; Geological Institute of Hungary—Kiadja a Magyar Állami Földtani Intézet: Budapest, Hungary, 2011; p. 180.
75. World Health Organization. *Determination of Airborne Fibre Number Concentrations; A Recommended Method, by Phase Contrast Optical Microscopy (Membrane Filter Method)*; World Health Organization: Geneva, Switzerland, 1997; pp. 1–53.
76. Anthony, J.W.; Bideaux, R.A.; Bladh, K.W.; Nichols, M.C. Handbook of Mineralogy. Available online: http://www.handbookofmineralogy.org (accessed on 26 August 2021).
77. Buthelezi, N. An Investigation into the Flotation Response of Wollastonite and Silicate Gangue Minerals. Master's Thesis, McGill University, Montreal, QC, Canada, January 2020.
78. Van Oss, C.J.; Giese, R.F. The hydrophilicity and hydrophobicity of clay minerals. *Clays Clay Miner.* **1995**, *43*, 474–477. [CrossRef]
79. Chan, J.X.; Wong, J.F.; Hassan, A.; Mohamad, Z.; Othman, N. Mechanical properties of wollastonite reinforced thermoplastic composites: A review. *Polym. Compos.* **2020**, *41*, 395–429. [CrossRef]
80. Yuhaida, I.; Salmah, H.; Hanafi, I.; Firuz, Z. The effect of acrylic acid on tensile and morphology properties of wollastonite filled high density polyethylene/natural rubber composites. *Procedia Chem.* **2016**, *19*, 401–405. [CrossRef]
81. Maxwell, D.C.; Hawthorne, F.C. A structure hierarchy for silicate minerals: Chain, ribbon, and tube silicates. *Min. Mag.* **2020**, *84*, 165–244.
82. Ohashi, Y.; Finger, L.W. The role of octahedral cations in pyroxenoid crystal chemistry; I, Bustamite, wollastonite, and the pectolite-schizolite-serandite series. *Am. Min.* **1978**, *63*, 274–288.
83. Matsueda, H. Iron-wollastonite from the Sampo mine showing properties distinct from those of wollastonite. *Min. J.* **1973**, *7*, 180–201. [CrossRef]
84. Nechita, M.T.; Berlier, G.; Ricchiardi, G.; Bordiga, S.; Zecchina, A. New precursor for the post-synthesis preparation of Fe-ZSM-5 zeolites with low iron content. *Catal. Lett.* **2005**, *103*, 33–41. [CrossRef]
85. Ohashi, T. Polysynthetically-twinned structures of enstatite and wollastonite. *Phys. Chem. Miner.* **1984**, *10*, 217–229. [CrossRef]
86. Rimstidt, J.D.; Dove, P.M. Mineral/solution reaction rates in a mixed flow reactor: Wollastonite hydrolysis. *Geochim. Cosmochim. Acta* **1986**, *50*, 2509–2516. [CrossRef]
87. Wollastonite NYAD G Technical Data Sheet. Available online: https://www.chem-on.com.sg/image/catalog/product_catalog/TDS%20-%20WOLLASTONITE%20NYAD%20G.pdf (accessed on 29 July 2021).
88. Droop, G.T.R. A general equation for estimating Fe^{3+} concentrations in ferromagnesian silicates and oxides from microprobe analyses, using stoichiometric criteria. *Mineral. Mag.* **1987**, *51*, 431–435. [CrossRef]

89. Gonda, I.; Abd El Khalik, A.F. On the calculation of aerodynamic diameters of fibers. *Aerosol. Sci. Tech.* **1985**, *4*, 233–238. [CrossRef]
90. Pollastri, S.; D'Acapito, F.; Trapananti, A.; Colantoni, I.; Andreozzi, G.B.; Gualtieri, A.F. The chemical environment of iron in mineral fibres. A combined X-ray absorption and Mössbauer spectroscopic study. *J. Hazard. Mater.* **2015**, *298*, 282–293. [CrossRef]
91. Pollastri, S.; Gualtieri, A.F.; Lassinantti Gualtieri, M.; Hanuskova, M.; Cavallo, A.; Gaudino, G. The zeta potential of mineral fibres. *J. Hazard. Mater.* **2014**, *276*, 469–479. [CrossRef] [PubMed]
92. Schott, J.; Pokrovsky, O.S.; Spalla, O.; Devreux, F.; Gloter, A.; Mielczarski, J.A. Formation, growth and transformation of leached layers during silicate minerals dissolution: The example of wollastonite. *Geochim. Cosmochim. Acta* **2012**, *98*, 259–281. [CrossRef]
93. Ptáček, P.; Nosková, M.; Brandštetr, J.; Šoukal, F.; Opravil, T. Mechanism and kinetics of wollastonite fibre dissolution in the aqueous solution of acetic acid. *Powder Technol.* **2011**, *206*, 338–344. [CrossRef]
94. Weissbart, E.J.; Rimstidt, J.D. Wollastonite: Incongruent dissolution and leached layer formation. *Geochim. Cosmochim. Acta* **2000**, *64*, 4007–4016. [CrossRef]
95. Xue, H.; Wang, G.; Hu, M.; Chen, B. Modification of wollastonite by acid treatment and alkali-induced redeposition for use as papermaking filler. *Powder Technol.* **2015**, *276*, 193–199. [CrossRef]
96. Peters, S.C.; Blum, J.D.; Driscoll, C.T.; Likens, G.E. Dissolution of wollastonite during the experimental manipulation of Hubbard Brook Watershed 1. *Biogeochemistry* **2004**, *67*, 309–329. [CrossRef]
97. Bellmann, B.; Muhle, H. Investigation of the biodurability of wollastonite and xonotlite. *Environ. Health Perspect.* **1994**, *102*, 191–195. [PubMed]
98. Macdonald, J.L.; Kane, A.B. Mesothelial cell proliferation and biopersistence of wollastonite and crocidolite asbestos fibers. *Fund. Appl. Toxicol.* **1997**, *38*, 173–183. [CrossRef] [PubMed]
99. Gualtieri, A.F. Bridging the gap between toxicity and carcinogenicity of mineral fibres by connecting the fibre crystal-chemical and physical parameters to the key characteristics of cancer. *Cur. Res. Toxicol.* **2021**, *2*, 42–52. [CrossRef]